Title
Neural correlates of perceptual decision making in primary somatosensory cortex

Authors
Alex G. Armstrong and Yurii Vlasov*

Affiliations
University of Illinois Urbana Champaign
Neuroscience Program
Electrical and Computer Engineering
Carle Illinois College of Medicine
Chan Zuckerberg Biohub Chicago

CONTACT INFO
*Corresponding author: Yurii Vlasov. Email: yvlasov@illinois.edu

Competing Interest Statement:
The authors declare that they have no competing interests.

Data Availability Statement. All data needed to evaluate the conclusions in the paper are present in the paper and/or the Supplementary Information. Datasets of electrophysiological and behavioral recordings are available at https://dandiarchive.org/dandiset/001341. Documentation on the behavioral virtual reality rig is available on GitHub: https://github.com/NeuroTechnologies/Tactile-VR-rig

This PDF file includes:
Main Text
Figures 1-4
Methods
Extended data Figures 1-10
References
Supplementary Information

Summary

The brain is thought to produce decisions by gradual accumulation of sensory evidence[1] through a hierarchically organized feedforward cascade of neuronal activities that transforms early stimulus representations in the primary somatosensory cortex (S1)[2] to a perceptual decision processed in pre-motor areas[3-6]. Recently, this prevailing view has been challenged by observation of choice-correlated neural activity as early in the hierarchy as S1[7-13]. Here, to reconcile these seemingly controversial observations, we employ ethological whisker-guided navigation of mice in a tactile virtual reality paradigm[14-16] combined with dense electrophysiological recordings in whisker-related wS1. Leaving only a pair of C2 whiskers for mice to navigate with, we effectively designed an information bottleneck for sensory input to decision making[16]. We show that neural activity in principal whisker wS1 barrel recorded during untrained and unrewarded two alternative forced choice (2AFC) decision-making consists of “fast” (50ms) and “slow” (200-300ms) stages that are mostly orthogonal to each other and directly precede the decision execution. The fast component represents detection of a deviant signal in sensory perception, that triggers dramatic collapse of the high-dimensional spiking activity to just a single latent variable followed by a slower and almost synchronous ramping up across the whole cortical column. We show that this variable is consistent with models of gradual accumulation of noisy sensory evidence to a decision bound[1,5,17,18]. These observations indicate that S1 may directly participate in a categorical coding of all-or-none decision variable via cortico-cortical feedback loops through which sensory information reverberates[17,18] to be transformed into perception and action.

Introduction

The prevailing view on perceptual decision making mostly based on influential research in the visual system of primates has been that sensory flow is gradually transformed from stimulus representations in the primary somatosensory cortex (S1)[2] to neural activity correlated with the decision in the secondary somatosensory cortex[19] (S2) up to a categorical all-or-none perceptual decision computed in pre-motor areas[3,4]. Here, close to the top of the cortical hierarchy, the internal decision variables are accumulated in a form of ramping neural activity[3-6] that is transformed into a decision when a decision boundary is reached[1].

Serial transformation of sensory inputs along the bottom-up hierarchical pathway has also been observed in rodents engaged in whisker-discrimination tasks[20,21] with an increasingly stronger association with perceptual choice in S2[22,23] and pre-motor areas[24-26] rather than whisker-related wS1[21]. The function of wS1 is usually analyzed[27] in the context of extraction of complex, high-order features of the sensory input[15,28,29]. It has been observed, however, that wS1 may integrate sensory information over time[7] and may contribute to goal-directed behavior[8,9]. A series of more recent experiments[10-13] have shown that neural activity in subpopulations of layer 2/3 of wS1 neurons is correlated with behavioral choice. In particular, wS1 neurons projecting to S2 were found to increase their spike rate, subsequently predicting the choice[10]. Correlation with choice was found to be the strongest for the feedback S2 to wS1 projecting neurons[11]. Hence these new findings, although seemingly contradicting earlier views, emphasize the role of feedback loops through which sensory information reverberates[18] to be transformed into perception and action.

Most decision-making studies in rodents, and in part, in primates, rely on stereotyped behavioral tasks that require intensive weeks-long training to obey artificial decision rules that may affect the underlying neural computations. To get further insights in processes of transformation of sensory inputs into perception and decision, it is crucial[30] to employ behavioral tasks that are much closer to animals' behavior in their natural habitat for which the brain circuits were specialized to deal with during evolution. Animal decision making is often associated with fast dynamics of navigating the terrain, outrunning predators, or pursuing prey that echoes fast ms-scale dynamics of "reverberations" of sensory information along the feedback loops. While 2-photon microscopy used in previous studies[10-13,15,22,23] can provide access to thousands of neurons simultaneously, it is typically limited to shallow cortical layers and has difficulty resolving fast neural dynamics.

Here, to address these challenges, we harnessed the natural whisker-guided navigation of mice using tactile virtual reality[14-16] combined with dense multielectrode array electrophysiological recordings. Head-fixed mice navigate at elevated speeds through a virtual corridor defined by a pair of motorized walls using only their whiskers that resembles closely navigation in burrows of their natural habitat[14]. As opposed to traditional trained designs, our task is untrained and unrewarded. Leaving only a pair of C2 whiskers for mice to navigate with, we effectively designed an information bottleneck for sensory input to decision making[16]. We strategically placed a microelectrode probe into the C2 principal whisker barrel and aligned it perpendicular to the cortical layers to record neural activity across the entire cortical column.

This design reveals unexpectedly strong correlation of neural activity across the columnar circuits with decision variables. In fact, during the decision formation the variance of the high-dimensional spiking activity collapses to just a single latent variable while spiking is synchronously ramping up across the whole cortical column. We show that this variable is consistent with models of gradual accumulation of noisy sensory evidence to a decision bound[1,5,17,18]. These observations indicate that primary sensory cortex not only retains relatively weak and sparce choice-related activity, as it was shown previously[7-13,22,23], but also, in our naturalistic behavioral task, directly participates in a categorical coding of all-or-none decision variable into which the majority of neural populations are recruited.

Results

Ethological decision-making during single-whisker-guided navigation in virtual reality

To load cortical circuits with difficult yet manageable cognitive tasks and at the same time elicit an ethologically relevant behavior, we designed a naturalistic tactile virtual reality[14-16] paradigm (Methods) in which head-fixed mice are running on a 3D treadmill, while navigating using only their whiskers (**Fig.1A**). The animal's movement in lateral (V_{lat}) and forward (V_{for}) directions is used to provide positive feedback to the movement of the walls (V_{wall}) positioned at both sides of the snout that generates a closed-loop (CL) virtual reality (VR) corridor for the animal to follow (**Fig.1B**). Importantly, all but just a pair of the C2 whiskers (second longest mystacial vibrissae oriented almost parallel to the ground) are trimmed, restricting the sensory information flow into the primary somatosensory cortex.

Typically, animals require only 3 days of habituation sessions with the CL straight trials (**Fig.1C**) to acclimatize to head-fixed locomotion (Methods) with water reward given only to encourage running at fast speed (21±4cm/s, mean ± s.d., **ED Fig.1A**). When habituated, animals are then used in a single terminal behavioral session that is unrewarded (**Fig.1C**) and lasts foup to 2 hours. To generate a two-alternative forced choice (2AFC) paradigm, we introduce an oddball deviant stimulus (open loop (OL) turn trials, **Fig.1D**). After a baseline CL straight section, the CL feedback signal is terminated, and the walls are first briefly removed beyond the reach of the C2 whiskers and then just one of the walls approaches the snout (within 0.2s) and stays at a pre-defined constant distance for 1.8 seconds before it retracts again (**Fig.1D**). Sensing fast-approaching obstacle from the left (or the right) with his left (or right) C2 whisker, the animal is forced to change the direction of the run (OL left or OL right turns, **Fig.1D**) to avoid the expected collision. Typical 20-seconds long trajectory of the animal locomotion is presented in **Fig.1E** exhibiting sections of straight runs (CL) and randomized left (OL_L) and right (OL_R) turns all performed while the animal is running at elevated speed.

We previously showed[16] that local ablation of less than 200 neurons in layer 4 (L4) of the principal C2 whisker barrel column, but not neighboring barrels, results in the inability of mice to produce turns guided by a whisker contra-lateral to the lesion, while still performing turns guided by ipsi-lateral whisker. Thus, we effectively created a bottleneck of the flow of sensory information critical for making decisions in our untrained and unrewarded 2AFC task.

Population dynamics in C2 barrel column exhibits strong, staged, and synchronous modulation during decision-making

For electrophysiological studies (Methods, **ED Fig.2**), either 64- or 960- channel (Neuropixel 1.0) multielectrode array probe (Supplementary information **(SI) Table 1**) was inserted in the C2 principal barrel column (Methods, **Fig.1F, G, H**) aligned perpendicular to the cortical layers. We use *Scnn1a-TG3-Cre* x *Ai32* transgenic line to enable targeting the principal barrel without use of stereotaxic surgery and enable optogenetic tagging (Methods). *In-vivo* fluorescent images of the brain exposed during surgery (**Fig.1F**) guide the insertion (**ED Fig.3A, B**). *Ex-vivo* histological mapping of the barrel cortex (**Fig.1G, ED Fig.3C, D**) and coronal slices (**Fig.1H, ED Fig.3E-H**) together with *in-vivo* optogenetic tagging and corresponding current source density (CSD) map (**Fig.1I**) confirms the probe placement and electrode assignment (Methods).

Trial-averaged population activity (Methods) for an example animal (#489, **SI Table 1**) is shown in **Fig.1J** and **Fig.1K** (other examples in **ED Fig.4**) for the OL_L left turns, where right wall approaches the snout while recording in the left hemisphere (contralateral turns, **Fig.1D**), and for the OL_R right turns where left wall approaches the snout instead (ipsilateral turns, **Fig.1D**), correspondingly. The spiking activity across all cortical layers is strongly modulated during approach (t=0s) and retraction (t=1.8s) of the walls and can roughly be divided into 5 consecutive epochs as shown in population-averaged (Methods) neural activity plots (**Fig.1L, M**). At the start of the turn when the wall is fast approaching (**Fig.1N**), a stable spiking (t<0s, 2±0.1Hz, mean ± s.d.) of epoch 1 is disrupted by a sharp peak of epoch 2 (t=0.026s) that is much stronger pronounced in a single L4 unit activity (**ED Fig.5A, B**) for both ipsi- and contra-lateral turns. Epoch 3 follows, exhibiting a strong

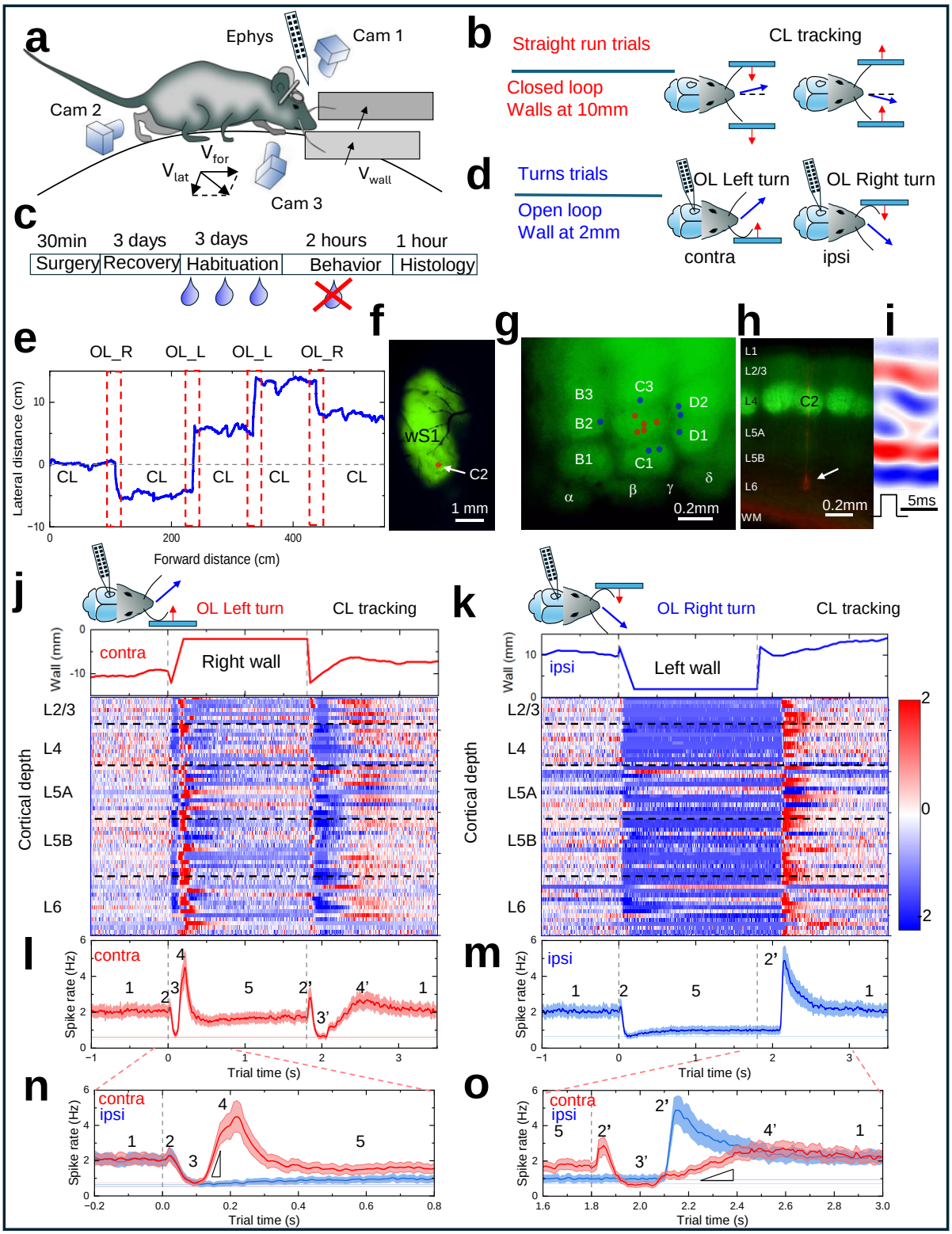

Figure 1. Neural activity in principal whisker barrel column exhibits strong, staged, and synchronous modulation during decision-making process.

Figure 1. Neural activity in principal whisker barrel column exhibits strong, staged, and synchronous modulation during decision-making process.

A) Schematics of single-whisker-guided virtual reality navigation experiments. Forward V_{for} and lateral V_{lat} speeds of animal locomotion on the air-suspended 16'-diameter sphere are used to calculate positive feedback signal V_{wall} that is fed into the motorized walls to approach or retract from the animal's snout. Additional high-speed cameras are used to track animal's legs as well as whisker interactions with the wall. Multielectrode array is implanted into the principal whisker barrel cortex to record single-unit electrophysiological activity.

B) In closed loop (CL) experiments when animal is navigating a straight VR corridor the distance between the wall and snout is set to 10mm with walls following the animal's trajectory in positive feedback closed loop.

C) Experimental protocol includes 2-3 days habituation in CL VR navigation as shown in B) when animal is rewarded for running at elevated speeds. This is followed by a single terminal experiment lasting for up to 2 hours where unrewarded and untrained 2AFC task with walls approaching the snout at 2mm distance are introduced in an open loop.

D) Open loop (OL) 2AFC task with right (contra-lateral to ephys probe) or left (ipsilateral) walls quickly approach the snout forcing animal to turn left (OL_L) or right (OL_R).

E) Example trajectory of animal navigating a randomized sequence of OL_L and OL_R turns separated by CL straight sections.

F) Fluorescence micrograph of a head-fixed animal after headbar attachment surgery with visible barrel cortex that is used for precise in vivo targeting of a principal whisker barrel.

G) Close-up view of a barrel cortex in fixed brain harvested immediately after the experiment. Locations of the probe entrance in the principal (red) and neighboring (blue) whisker barrels reconstructed from histology.

H) Superimposed green and red color fluorescence micrographs of a coronal slice though a principal whisker barrel column (animal 489) showing a probe track (red) and a microlesion (arrow) used for reconstruction of each electrode's locations.

I) Current-source density (CSD) trace following brief optogenetic activation used to register the location of layer 4 along the probe.

J) Top panel: Right wall position during the OL_L turn. Bottom: Trial-averaged z-scored spiking activity of 65 individual simultaneously recorded units (animal 489) across the principal barrel column for 266 OL_L left turns. Units are ordered by cortical depth and assigned to cortical layers.

K) Top panel: Left wall position during the OL_R turn. Bottom: Same as J) for 265 OL_R right turns.

L) Population-averaged spike rate for data in J) for OL_L left turns. Numbers correspond to modulation epochs 1 through 5. Red curve is population mean. Red error band corresponds to mean ± s.e.m. Vertical dotted line corresponds to the start of the wall movement.

M) Same as in L) for data in K) for OL_R right turns.

N) Population-averaged spike rates from L) and M) for the first 1 sec of turn trials. Vertical dotted line corresponds to the start of the wall movement. Red (blue) curves correspond to left (right) turns. Black triangle shows linear fitting of the ramping slope.

O) Same as in N) but for the last 1.4 sec of turn trials. Black triangle shows linear fitting of the ramping slope.

suppression of spiking activity down to 0.7 Hz ± 0.1 (mean ± s.d.) for both left and right turns (**Fig.1N**). While for ipsilateral turns the suppression lasts until the turn end (t=1.8s, blue curve in **Fig.1O**), the contralateral turns produce strong ramping activity of epoch 4 (t=0.25s, red curve in **Fig.1N**) that is quenched at longer times to a stable epoch 5 until the turn end (t=1.8s, red curve in **Fig.1O**). Here, similar staged modulation is observed (**Fig.1O**) when both contra-lateral and ipsi-lateral walls are moving back to 10mm distance to resume CL wall tracking (at t>2s). Importantly, all 5 epochs are the major features that dominate the neural activity for each of individual 65 simultaneously recorded units (single unit examples in **ED Fig.5**) that are highly reproducible across 531 randomized trials with jitter of just 30ms.

Overall, both single unit and the population-averaged spike rates represent strong, staged, and almost synchronous modulation across the principal barrel column. Such synchronization of firing across the cortical column is a commonly observed phenomena[31] during decision making that is attributed to top-down feedback regulation[32,33] that influences experience-derived predictions[10], establishment of attentional state[34] and working memory[35]. In what follows, we will argue that these distinct epochs of neural modulation are strongly correlated with different behavioral stages of the decision-making process.

Behavioral correlates of decision-making mark the duration of a choice period

To extract the behavioral measures and correlates of decision making such as the start of choice-relevant sensory input, motor action execution of the choice, associated reaction times (RT), and psychometric curves, we analyzed the statistics of animal trajectories, velocities, and accelerations (n=7). Trajectories for 414 consecutive randomized left and right turn trials for an example animal (#503, other examples in **ED Fig.6A, B**) are shown in **Fig.2A**. While straight CL section produces trajectories very tightly confined within 0.14 cm ± 0.55 (mean ± s.d.) (**Fig.2B**, bottom histogram at t=0s), the distributions of lateral distances after the turn are widening over time (**Fig.2B**, middle at t=1s, and top at t=3s) indicating gradual accumulation of navigation uncertainties. If a threshold for correct trials is defined as ±1cm lateral clearance at t=1s, the success rate for this animal is reaching 95% (14 failed red trajectories in **Fig.2A**). To measure psychometric curves a set of additional experiments was performed (n=7, Methods, **ED Fig.6E, F, G**) with the lateral distance in the OL turn trials varied from 8mm (whisker barely touching the wall) to 1mm (whisker strongly bent by the wall). The resulting success rate as a function of wall distance (**Fig.2C**) exhibits a strong increase towards shorter distances. Better threshold clearance is achieved by steeper turn angles (**Fig.2D**) at closer wall distances[14] reflecting the stronger evidence for the animal to turn faster to avoid the anticipated collision[16].

Since the only sensory cue that animals are provided with to navigate the turns is whisking, we tracked the contra-lateral (right) C2 whisker (**Fig.2E**) with high-speed overhead camera (Cam1 in **Fig.1A**, 1000fps) while it interacts with the wall approaching the snout. Whisker angles (**Fig.2F**, middle) and curvatures (**Fig.2F**, bottom), as well as whisker touch times (**Fig.2F**, red dots) are extracted from the videos (Methods). Whisking during the CL straight run (t<0) is executed at 18±4Hz (mean ± s.d.) with an amplitude of just 20° ± 5 (mean ± s.d.) around a set point of 58° ± 5 (mean ± s.d.) that is typical for a “foveal” whisking generated during fast locomotion[14,20]. In this foveal mode, a whisker periodically palpates the surface during short 50ms touches[27] (**Fig.2F**, red dots) occurring mostly during retraction cycles. When the wall is at the close proximity, the whisking amplitude is restricted (whisker angle is clamped at 48° ± 5 (mean ± s.d.) for t>0.2s in **Fig.2F**, middle). However, the curvature is still strongly modulated (**Fig.2F**, bottom) indicating that whisking action remains intact. The first touch (FT) of the whisker to the approaching wall is detected at t=0.07s (red arrow in **Fig.2F**, middle) indicating the very first moment when the animal starts receiving new information that one of the walls is suddenly fast approaching.

The time of decision execution is extracted from the analysis of videography data (**Fig.2G**) using two additional side cameras (Cam2 and Cam3 in **Fig.1A**) that reveals moments when the right and left fore (RF and LF) and hind (RH and LH) legs are touching the ground (**Fig.2H**, bottom, **SI**

Video 1). Characteristic coordinated sequence of diagonal LH-RF and RH-LF strides observed corresponds to trotting, the natural gait that animal is producing[36] to accommodate speeds faster than 20cm/s. Individual strides are also detected as consistent periodic oscillations[14] in run angle derivative (**Fig.2H**, middle) with maximum positive (turning left) peak at t=0.29s (**Fig.2H**, middle, red arrow). Comparison with the gait reconstruction indicates that the left turn is executed by the stereotypic push (**Fig.2G**, right, red arrow) provided by the RH leg (red arrow in **Fig.2H**, middle). This peak in angle derivative (Methods) is repetitive for all 414 trials for both left and right turns (**ED Fig.7**) and is used to extract the trial reaction time (RT). Corresponding time histograms for the FT and the RT (**Fig.2I**) indicate the choice period of 0.32s between the mean FT (0.06 s ± 0.03, mean ± s.d.) and the mean RT (0.38 s ± 0.07, mean ± s.d.).

Stages of decision-making strongly correlate with epochs of neural activity modulation.
During epoch 1 both contra- and ipsi-lateral whiskers are periodically palpating walls (**Fig.2F**, middle, red dots) providing continuous in-flow of sensory information to enable CL wall tracking[16]. Similarly, during epoch 5, periodically varying sensory inputs are generated by oscillating whisker curvature (**Fig.2F,** bottom). However, for both epochs, a nearly stationary neural activity is observed for both population- and trial-averaged activity (**Fig.1J,K**) as well as for a single unit activity highly reproducible for all trials (**ED Fig.5**) that indicates strong adaptation[29] of neural population to these repetitive palpating events. While stable during these epochs, the population activity exhibits high variability at ms-scale. As revealed by multi-parameter generalized linear-nonlinear Poisson model[37] (GLM) analysis (Methods), the population variance represents high-dimensional latent variables (**Fig.2J**). Not only whisking kinetics (i.e. angle, phase, amplitude) and kinematics (i.e. curvature) are strongly represented, but also behavioral variables related to animal movement and gait. Such mixed high-dimensional representations were observed previously in spontaneous brain-wide activity even without external sensory input indicating sensory-motor integration as early as primary visual cortex[38]. In our case such fusion of sensory (whisker related) and behavioral (motor-related) information encoding in the barrel cortex may help active whisker-guided navigation that requires continuous inference[16] of relative positions of the obstacle (approaching wall sensed by whisking) and the mouse body (sensed by proprioception) to estimate the time to collision. It is not surprising then that the strongest correlation (R^2 = 0.79) is observed for the feedback signal V_{wall} that is driving the walls in our VR and is dictated by the animal navigation to avoid the collision.

In contrast to adapted stable spiking during epochs 1 and 5, just a single touch of a contra-lateral whisker to an approaching wall at FT (**Fig.2E**, middle, t=0.07s) matches closely a strong increase of neural activity during epoch 2 (**Fig.2K**). Note that a similar peak (peak 2' in **Fig.1O**) is also observed at the end of the trial at t=1.84s, that appears in both population-averaged activity (**Fig.1O**) and single unit response (**ED Fig.5**). Here, at the trial end, a clamped whisker is released, returning to full range of whisking when the right wall starts to retract (**ED Fig.8A**). Therefore, epochs 2 and 2' peaks are likely associated with coding of the mismatch signal[39] notifying the downstream circuits on the appearance of a sudden deviance[40] in the sensory flow. This is supported by observation of similar peaks during right turns (**Fig.1O, ED Fig.5**) that match the FT of ipsi-lateral whisker last touch of the retracting (t=0.06s, epoch 2) and first touch of the approaching (2.15s, epoch 2') left wall. In all cases the epoch 2 peaks appear within 10ms range from FT consistent with functional afferent delay from whisker follicle to the barrel cortex[41].

Peak 4 activity is separated from peak 2 by a large suppression dip of epoch 3 and is delayed by almost 200ms relative to the FT that exceeds possible afferent delays. Peak 4 activity is ramping up and reaches its maximum while the periodic wall-palpating events continue even when the wall starts to approach (2-3 wall touches on average, **Fig.2F**, middle) until the whisker is clamped at t=0.2s. Hence, it seems unlikely that activity ramping during such nearly stationary sensory input can be attributed directly to purely sensory modulation. To further identify the origin of peak 4, we analyzed experiments from an animal (#480) that spent nearly equal time running and sitting (**Fig.2K**). While peak 2 is dominant for both ipsi- (**Fig.2K**, blue) and contra-lateral (**Fig.2K**, black) turns when the animal is passively sitting while whiskers are palpating the approaching wall, peak 4

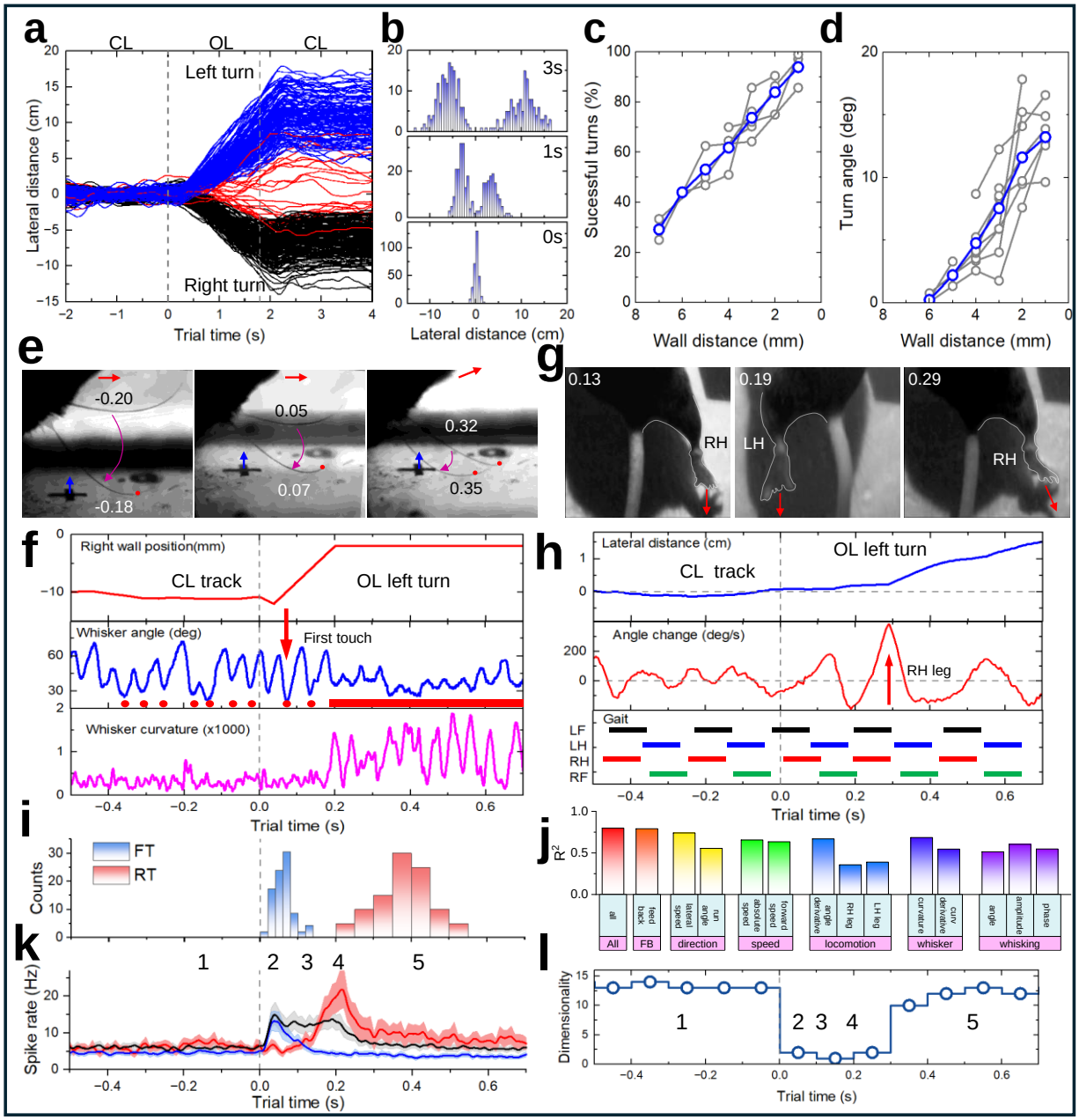

Figure 2. Stages of decision making strongly correlate with stages of neural activity modulation.

A) Trajectories for 414 trials randomized between OL_L left (blue) and OL_R right (green) turns (animal 503). Red curves correspond to trials assigned to decision errors. Vertical dashed lines correspond to histograms in B).

B) Histograms of lateral distance distributions at t=0s (bottom), t=1s (middle), and t=3s (top). While at the beginning of a turn the lateral distribution is narrow, they broaden, indicating gradual accumulation of navigation uncertainties.

C) Percentage of success trials as a function of the wall distance during OL experiments. Psychometric curves are measured for left and right turns for different animals (n=4, gray, minimum 20 trials per distance) and their population average (blue).

D) Mean turn angle for the same data as in C) (n=4).

E) Series of a pair of superimposed still frames from a high-speed video of Cam1 (**SI Video1**) showing whisking for several time stamps during CL straight run (left), first touch to approaching wall (middle), and during OL interaction at constant wall position during turn (right). Red dots correspond to whisker touching the wall. Red arrow shows direction of mouse run, blue arrows show direction of wall movement.

F) Top panel: Position of the right wall during the left turn. Middle panel: extracted whisker angle. Red dots

identify moments of whisker touching the wall, with the first touch to approaching wall marked by the arrow. Bottom panel: Same for extracted whisker curvature. Vertical dotted line corresponds to the start of the wall movement.

G) Series of still frames from a video taken by camera Cam2 (**SI Video1**) tracking positions of hind legs during 3 consecutive strides corresponding to decision execution (Animal 589). Red arrows show direction of the push. Timestamps correspond to angle change maxima in H).

H) Top panel: Lateral distance during the left turn trial (Animal 589). Middle panel: Angle change curve with a stereotypic RH leg push at beginning of turn corresponding to G) at t=0.37s. Bottom panel: tracked left and right hind and fore legs following diagonal trotting gait pattern.

I) Histograms of first whisker touch (FT, blue) and reaction time defined by stereotypic RH leg push (RT, red) extracted from recordings similar to F) and H) for animals 573 and 480, respectively.

J) Multiparameter generalized linear-nonlinear Poisson model (GLM) fitting of spiking activity during 55 CL straight run trials (animal 579, 34 units). Vertical axis is bootstrapped R^2. Parameters are grouped by locomotion variables (direction, speed and gait) and sensory variables (whisker kinetics and kinematics). FB corresponds to a feedback signal V_{wall} that drives the closed loop VR.

K) Population averaged spike rate (animal 480) for OL_L left turn trials recorded when animal was sitting (177 trials, black) and running (96 trials, red). Blue curve is for OL_R trials for reference. Error band corresponds to mean ± s. e. m. Vertical dotted line corresponds to the start of the wall movement

L) Intrinsic dimensionality of the neuron population during the OL_L left turn trial (animal 489). Dimensionality refers to the number of latent variables required to explain at least 90% of the variance of the neural data, showing collapse to a single latent variable during the choice period.

activity dominates the modulation only when the animal is engaged in active whisker-guided navigation (**Fig.2K**, red). Hence peak 4 is likely to reflect participation of primary somatosensory cortex in motor preparatory activity often observed in higher pre-motor cortices[24-26]. Indeed, peak 4 starts after FT (**Fig.2I**, blue), reaches maximum at the start of RT (**Fig.2I**, red), and is quenched when the decision is fully executed while stimulus signals continue to arrive (**Fig.2F**).

Analysis of intrinsic dimensionality[42] (Methods) of population activity during decision making (**Fig.2L**) confirms high-dimensionality during epoch 1 that collapses rapidly to just a single dimension following the FT. Decline of spiking variability at the sensory onset is a known universal cortical phenomenon assigned to stabilization of a network state[43]. However, in our experiments the neural population activity remains one-dimensional[44] during the whole choice period between FT and RT and starts to increase only at the onset of decision execution and in epoch 5. The emergence of synchronous modulation[32,33], dimensionality collapse[44], and strong suppression locked to sensory stimulation[45,46] are all known neural correlates of top-down regulated attention[34] and decision making processes[3-5]. In what follows we will argue that the neural activity ramp during epoch 4 is consistent with a bounded integration mechanism of decision making[1,3-5].

Ramping neural activity reflects temporal accumulation of sensory evidence

A canonical framework of perceptual decision making[1] considers the decision process as the linear integration of evidence over time during sequential noisy sensory sampling until a decision bound is reached. A decision variable (DV) in a standard drift-diffusion model (DDM)[1,3-5] (**Fig.3A**) accumulates sensory evidence (drift) accompanied by a stochastic internal or sensory noise (diffusion) that, when reaches either upper (correct trials) or lower (error trials) bound, produces a decision at RT. Fitting the classical DDM model (Methods) to the experimental distribution of RT (**Fig.3B**) produces the best fit (Bayesian information criterion, BIC of -664, **Fig.3C**) for the non-decision time (NDT) of 0.11s (**Fig.3D**), drift K=2.91, bound B=0.59 (**Fig.3E**), and noise σ=0.25 (**SI Table.2**). Similar parameters are extracted from fitting a “full” DDM model that includes variability of initial conditions X_0 and of NDT. Noticeably, the appreciable NDT from both DDM and “full” DDM (**Fig.3D**) fits well to 0.12s delay of experimentally observed ramping onset at the end of epoch 3 for this example animal (**Fig.3B**, bottom, up red arrow). The DDM is known to be suboptimal, especially when evidence strength varies as in the case of whiskers periodically palpating the surface. To accommodate this, we introduced additional model components (Generalized DDM model[47]) including exponentially collapsing bounds[6] and a leaky integrator[17] that produce a slightly better fit (BIC of -705). The normalized drift K/B that defines the time needed to reach the bound in the absence of noise and decay is 11.12. This is noticeably close to the linear slope of the ramping peak 4 of 12.25 ± 0.88 (mean ± s. e. m.) (**Fig.3B**, bottom, black triangle) for this example animal (other examples in **ED Fig.9** and **Fig.4E** below, n=7, 13.05 ± 4.59, mean ± s.d.). These observations enable us to hypothesize that the onset of ramping activity at 0.12s may indicate the decision onset (**Fig.3B**, bottom, up red arrow), while the linear ramping of peak 4 reflects the accumulation of evidence until the decision is reached (**Fig.3B**, bottom, down red arrow). Thus, a single variable dominating population dimensionality during the choice period (**Fig.2L**) may reflect a linearly increasing DV that is reset at the end of epoch 4 when the decision is reached and executed[48].

Important diagnostic signature of perceptual decision-making is gradual accumulation of noise[5,49] expected for most accumulation-to-bound decision models. The total variance of this doubly stochastics process becomes a sum of two separate components[49] (Methods): point process variance (PPV) that is proportional to mean spike rates and variance of conditional expectation (varCE) that reflects the variance of rates. For an example unit (**ED Fig.10A**) the total variance (**Fig. 3F**, black) follows the PPV (**Fig. 3F**, blue) for epochs 1 through 3, but saturates for epoch 4 while the PPV is fast ramping up. The resulting varCE (**Fig. 3F**, red) exhibits a fast increase at the beginning of epoch 4 indicating accumulation of stochastic trial-by-trial diffusion noise[5,49]. This unit, however, is an outlier as it has the highest spiking rate and hence generates abundant noise. When varCE is calculated for each unit in the population (**Fig.3H**) some indeed contribute the most (**Fig.3I**). However, the shape of the population-averaged varCE (**Fig.3G**, blue) is similar to that with outliers

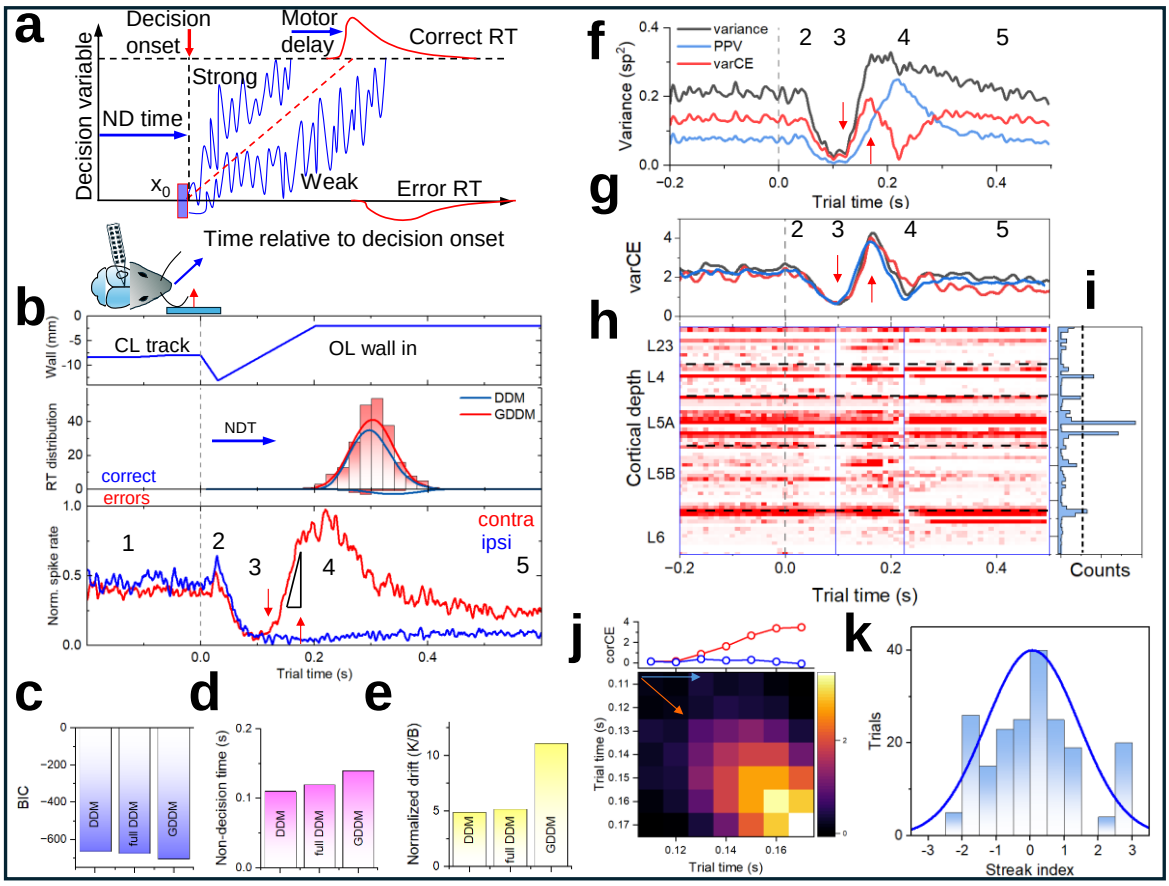

Figure 3. Ramping neural activity reflects temporal accumulation of sensory evidence.
A) Schematics of the drift-diffusion model (DDM) of perceptual decision making. Blue curves are single trial trajectories of a decision variable (DV). The trajectories are affected by a constant drift (dashed red line) and subject to stochastic diffusion noise. The decision process starts at delay related to the non-decision time (NDT) and is finished when the DV is reaching the upper (correct trials) or lower (error trials) bounds. X0 denotes initial bias in DV. RT are delayed beyond the DV reaching the bound by motor related efferent delay.
B) Top panel: Position of the right wall during OL_L left turn trials. Middle: RT distribution (animal 489) fitted by DDM (blue) and Generalized DDM (GDDM, red) models. Both produce the similar NDT time about 0.12s shown by blue arrow. Bottom: Normalized spike rate for 266 contralateral (contra, red) left and 265 ipsilateral (ipsi, blue) right turn trials (animal 489). Up and down arrows denote times for the beginning and the end of the linear ramping activity. Black triangle shows linear fitting of the ramping slope.
C) Bayesian information criterion (BIC) for three fitted models – DDM, full DDM and GDDM.
D) Non-decision time derived from DDM, full DDM, and GDDM fits to the RT.
E) Drift normalized on bound derived from DDM, full DDM, and GDDM fits to the RT.
F) Total variance (black), PPV (blue) and varCE (red) for a single unit (489101, RS, layer 5A, animal 489). Arrows mark the start and the end of the linear ramping activity from B).
G) varCE variance calculated for all units in animal 489 (blue), with outliers taken out (red), and calculated on residuals (black). For the same 266 OL_L trials.
H) Trial averaged activity plot of varCE for all units (animal 489) ordered by cortical depth and assigned to cortical layers.
I) The sum of varCE calculated for all units in H) for a trial time corresponding to a choice period (blue lines in H). Dashed black line defines 4 outliers.
J) Covariance matrix CorCE calculated on residuals. Top: corCE values along the matirx diagonal (red) and along the top row (blue).
K) Streak index distribution for all units across all trials. Blue curve is normal distribution fit.

taken out (**Fig.3G**, red). When varCE is calculated from residuals[5,49] (Methods), it appears also very similar (**Fig.3G**, black) showing linear increase between the decision onset (**Fig.3G**, up arrow) and decision termination (**Fig.3G**, down arrow) times. VarCE exhibits a fast decline at the end of the decision process reaching minimum at t=0.23 when the decision starts to be executed. Overall, varCE exhibits a linear increase during epoch 4 that is a characteristic signature of a diffusion process consistent with accumulation-to-bound decision model[5,49].

It has been argued[49] that if variance of spike rates during evidence accumulation are defined by a diffusion process, then the expectation of spike counts in consecutive time bins (CorCE) should co-vary. The calculated (Methods) CorCE matrix (**Fig.3J**) indeed exhibits characteristic increase of correlation as a function of time (along the diagonal) and, for a given time (e.g. along the top row), shows sequential decay as often observed[5,49] during the decision making process. This correlation disappears when the bins are randomly shuffled (**ED Fig.10B**). Together, the time course of CorCE and linear increase of VarCE is indicative of accumulation of evidence during linear ramping in epoch 4. In addition, we performed streak index analysis[50] on a trial-by-trial basis[51] (**ED Fig.10C**, Methods) that shows randomness of local spike count fluctuations with close to zero mean (0.06 ± 1.36, mean ± s.d., **Fig.3K**) indicating gradual rather than step-like transition in each trial during ramping.

Discussion

Summarizing the argumentation presented above, the epoch 4 ramping of neural activity arises at delays that are considerably longer than sensory afferent delays. Ramping occurs while the sensory input stays nearly stationary. Ramping reaches its maximum and starts to decay during the onset of motor decision execution at RT while stimulus signals continue to arrive. Epochs 3 and 4 are accompanied by drastic collapse of high-dimensional neural activity to a single latent variable. Fitting of the RT distributions to the bounded accumulation models (DDM, GDDM) reveals that this single variable is consistent with the linear evidence accumulation of DV. Fitted drift slopes and non-decision times in behavior data are consistent with observed ramping slope and ramping delay in recorded neural activity. Analysis of spike count noise during this period showed characteristic linear increase in internally driven spike rate variability (varCE) and decrease of its correlations (corCE) consistent with the gradual accumulation models of decision making[49]. Streak index analysis[50,51] also supports this interpretation. Overall, these 9 arguments provide evidence that epochs in modulated neural activity observed during active single-whisker-guided navigation are likely to represent stages of perceptual decision making.

The first-pass prediction of the accumulation to bound models is that the ramping slope should be decreasing with the decrease of the stimulus strength. To test this experimentally, we focused on the second part of the trial when the contra-lateral wall starts to move out (t=1.8s) from being at 1mm proximity to the snout to 10mm mean distance during the subsequent CL wall tracking (**Fig.1J**, top). Epoch 2' peak coincides with the release of the contra-lateral whisker from being strongly bent during the turn (**ED Fig.8A**), that corresponds effectively to the lower part of the psychometric curve (**Fig.2C**). Epoch 3' suppression is significantly longer with the onset of ramping activity at t=2.0s (0.21s delay) suggesting regulation of integration onset to task demand. Ramping in epoch 4' is also much slower reaching maximum at t=2.58s (0.78s delay). The fitted linear slope (2.05 ± 0.05, mean ± s.e.m., black triangle in **Fig.1O**) is about 7X smaller than for the first turn at the trial start (12.25 ± 0.76, mean ± s.e.m., black triangle **Fig.1N**) consistent with drift-diffusion model prediction. Similarly, accumulation to bound models predict that decrease of the stimulus strength should be accompanied by accumulation of larger uncertainties in decision making (**Fig.3A**), consistent with observed 2X wider distribution of lateral distances at the trial end relative to the trial middle (2.30 s.d. at 3 s trial time vs 1.49 s.d. at 2 s time for **Fig.2B**, top, see also **ED Fig.6B**, top). Slower ramping is also accompanied by longer and broader distribution of angle derivative peaks (**ED Fig.8D**) although exact identification of RT is difficult as the decision execution is distributed among several consecutive strides.

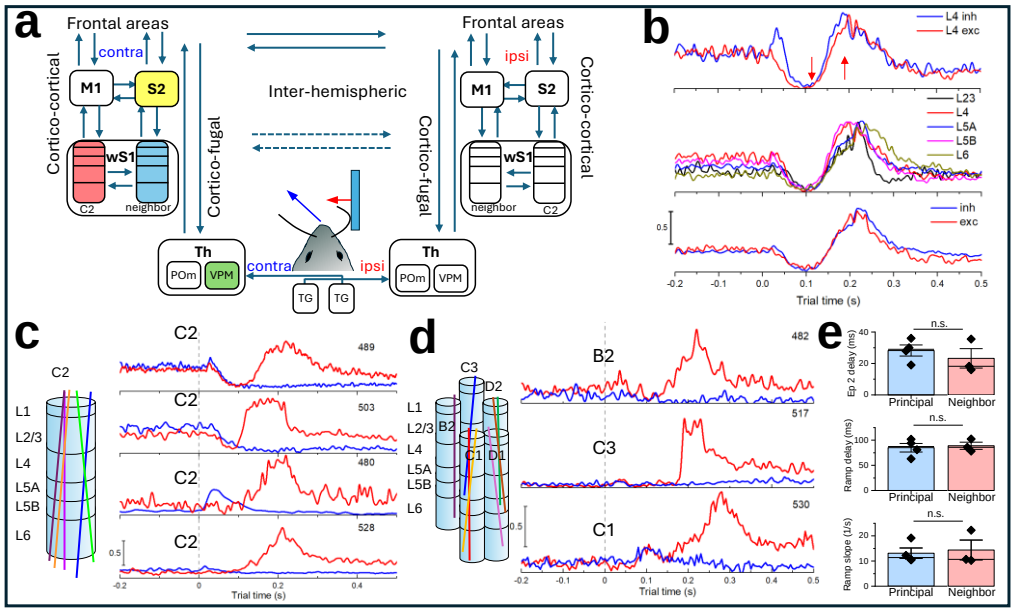

Figure 4. Accumulation of evidence is likely generated not locally but is provided by feedback.
A) Schematics of ascending and descending pathways in a whisker somatosensory system.
It starts with characteristic isomorphic representation of the whiskers via barrelettes in ipsilateral brainstem trigeminal (TG) nuclei, then crosses to barreloids in contralateral thalamic (Th) posterior thalamic (POm) and ventroposterior medial thalamic (VPM) nuclei, which project to primary S1 and secondary S2 somatosensory cortices as well as motor areas (M1). Primary (wS1) and secondary (S2) vibrissae cortical areas have strong reciprocal connections to Th and between themselves. While direct interhemispheric connections exist between contra- and ipsi-lateral S1 and S2, they are much stronger in higher order cortices.
B) Top panel: Normalized spike rates of the subpopulations of FS (blue) and RS (red) units in layer 4 (animal 489). Middle: Same for subpopulations of units in different cortical layers (L2/3 = 10 units, L4 = 13, L5A = 13, L5B = 16, L6 = 13). Bottom: Same for all FS (blue, 43) and RS (red, 22) units.
C) Left: Schematics of reconstructed probe positions for n=4 animals where recording was done in the C2 principal whisker barrel (corresponding to red dots in Fig.1G). Population-averaged spike rate for these animals with red curves corresponding to the left OL_L left turn trials, while blue curves to the OL_R right turns. Details for each recording in Table S1.
D) Left: Schematics of reconstructed probe positions for n=3 animals where recording was done in the whisker barrels neighboring the C2 (corresponding to blue dots in Fig.1G). Population-averaged spike rate for these animals with red curves corresponding to the left OL_L left turn trials, while blue curves to the OL_R right turns. Details for each recording in Table S1.
E) Statistical comparison of the epoch 2 delay (top), delay of ramping activity (middle), and linear regression slope (bottom) extracted from recordings in the principal (left, blue) and neighboring (right, red) barrels. Data are represented as mean ± s.e.m.; n.s., not significant (p>0.05), two-sample t-test (top = 0.109, middle = 0.140, bottom = 0.970).

Where are these computations taking place? Most information about whisker contact with objects is relayed through the main lemniscal pathway[20,27,41] (**Fig.4A**). Can the ramping signal be computed locally within a principal barrel column in primary wS1 (**Fig.4A**, red)? All epochs including epochs 3 and 4 are already present in thalamo-recipient Layer 4 populations of fast spiking (FS, putative inhibitory, **Fig.4B,** top) and regular spiking (RS, putative excitatory, **Fig.4B,** top) units. They are also dominating the activity in sub-populations of all units across different cortical laminae (**Fig.4B**, middle panel) and sub-populations of all excitatory and inhibitory units (**Fig.4B**, bottom panel). Similar synchronous modulation of neural activity is observed for additional cohort of animals (n=4, **Fig.4C**) with recordings from the principal barrel column indicating that the coding scheme behind epochs 3 and 4 is unlikely to be produced by local columnar circuitry but is rather regulated from the outside of the principal whisker column.

Can the epoch 3 and 4 modulation involve surround/lateral inhibition[52] from neighboring barrels columns[53] (**Fig.4A**, blue)? Strong cross-columnar excitatory long-range axon collaterals connect neighboring columns running predominantly along the barrel rows[54]. However, staged and synchronous modulation epochs observed in animals where recordings were performed from a neighboring barrel in the same or even different row (n=3, **Fig.4D**), exhibits a striking similarity indicating that lateral cross-columnar inhibition[53] is unlikely a source. Indeed, delay of epoch 2 (**Fig.4E**, left), start of ramping at the end of epoch 3 (**Fig.4E**, middle) and a linear slope of ramping activity of epoch 4 (**Fig.4E**, right) shows no statistically significant difference (two sample t-test, $p>0.05$) between the principal C2 whisker and neighboring barrel columns. This agrees with the conjecture that the coding scheme behind epochs 3 and 4 is unlikely to be produced within a barrel cortex, but rather is a signature of a global feedback regulation.

If the modulation of epochs 3 and 4 is not generated locally, where can it arise from? Can it be generated by cortico-thalamo-cortical feedback loops[55,56] (**Fig.4A**, green) or initiated downstream in higher order cortices like S2 (**Fig.4A**, yellow) or even hierarchically higher frontal areas and then top-down regulated back into S1? Some clues can be learned from observation of remarkable inter-hemispheric asymmetry in contra-lateral (left turns) and ipsi-lateral (right turns) trials (**Fig.4CD**, see also **Fig.1J-O**). While epochs 2 (at trial start) and 2' (at trial end) are present for both left and right turns, epochs 4 and 4' ramping is observed exclusively for contra-lateral left turn trials indicating extraordinarily strong lateralization. Therefore, this global regulation is unlikely to originate directly from frontal cortical pre-motor areas[24-26] since frontal cortices have a very high degree of symmetry for both ipsilateral and contralateral projections[57]. In contrast, sensory S1 and S2 cortices have strongly lateralized ipsilateral outputs[41,57] and are densely and reciprocally interconnected[58] forming a top-down feedback loop that exhibits choice-related activity[10-13,22,23].

Similarly, cortico-fugal[59,60] and, more specifically, cortico-thalamo-cortical[55,56] organization is also mainly ipsilateral and is known to form feedback loops. For example, posterior thalamic nucleus (POm) may provide a thalamic relay for cortico-cortical information flow between S1 and S2 sensory areas[55] and was shown recently to be indispensable in whisker-based texture discrimination tasks[56]. Therefore, both cortico-cortical and cortico-fugal feedback loops are likely to contribute to the observed modulation epochs. Our experiments indicate, however, that contra-lateral activity of peak 4' continues ramping unperturbed at the trial end (**Fig.1O**, red) when the ipsi-lateral whisker is touching the approaching wall (t=2.16s, 0.36s delay from the onset of wall movement) to generate a strong peak 2' (**Fig.1O**, blue). This indicates that two processes are likely evolve orthogonal to each other, hence originating from different loops. Our findings are consistent with the hypothesis that "early"[8,9] sensory response (peak 2 in our case) is mostly perception-related and may rely on thalamo-cortico-thalamic loops[56], while "late" mostly decision-related response[7] (peak 4 in our experiments) reflect reverberation of neural activity[17,18] in cortico-cortical S1-S2 loops[10-12,22,23].

A limitation of our approach is that we focused on analysis of decision-related activity exclusively from the primary S1 area. However, our experiments produce intriguing observations pointing to architectural organization of feedback cortico-cortical and cortico-fugal loops that contribute to observed decision-related ramping activity in S1. To study transformations of sensory inputs to decision-related variables would require simultaneous recording from multiple areas

potentially involved in a feedback regulation as has been implemented recently[10-12,22,23]. We demonstrated here that recording of such dense neural activity datasets during our single-whisker-guided ethological decision-making behavioral paradigm is a powerful approach for mechanistic dissection of these complex nested loops. Our work therefore offers a key step toward understanding the contribution of early sensory cortical circuits to decision making during natural behavior.

Acknowledgements

YV is a CZ Biohub Investigator. Authors are grateful to Kun Hu and Nur Al-Kodmany for help in setting up the VR rig and development of behavioral protocol and to Ksenia V. for insightful discussions.

References

1 Ratcliff, R., Smith, P. L., Brown, S. D. & McKoon, G. Diffusion Decision Model: Current Issues and History. *Trends in Cognitive Sciences* **20**, 260-281 (2016). https://doi.org:10.1016/j.tics.2016.01.007

2 Hernández, A., Zainos, A. & Romo, R. Neuronal correlates of sensory discrimination in the somatosensory cortex. *Proceedings of the National Academy of Sciences* **97**, 6191-6196 (2000). https://doi.org:doi:10.1073/pnas.120018597

3 Roitman, J. D. & Shadlen, M. N. Response of Neurons in the Lateral Intraparietal Area during a Combined Visual Discrimination Reaction Time Task. *The Journal of Neuroscience* **22**, 9475 (2002). https://doi.org:10.1523/JNEUROSCI.22-21-09475.2002

4 Gold, J. I. & Shadlen, M. N. The Neural Basis of Decision Making. *Annual Review of Neuroscience* **30**, 535-574 (2007). https://doi.org:10.1146/annurev.neuro.29.051605.113038

5 de Lafuente, V., Jazayeri, M. & Shadlen, M. N. Representation of Accumulating Evidence for a Decision in Two Parietal Areas. *The Journal of Neuroscience* **35**, 4306-4318 (2015). https://doi.org:10.1523/jneurosci.2451-14.2015

6 Churchland, A. K., Kiani, R. & Shadlen, M. N. Decision-making with multiple alternatives. *Nature Neuroscience* **11**, 693-702 (2008). https://doi.org:10.1038/nn.2123

7 McGuire, L. M. *et al.* Short Time-Scale Sensory Coding in S1 during Discrimination of Whisker Vibrotactile Sequences. *PLoS Biol* **14**, e1002549 (2016). https://doi.org:10.1371/journal.pbio.1002549

8 Yamashita, T. & Petersen, C. C. H. Target-specific membrane potential dynamics of neocortical projection neurons during goal-directed behavior. *eLife* **5**, e15798 (2016). https://doi.org:10.7554/eLife.15798

9 Sachidhanandam, S., Sreenivasan, V., Kyriakatos, A., Kremer, Y. & Petersen, C. C. H. Membrane potential correlates of sensory perception in mouse barrel cortex. *Nature Neuroscience* **16**, 1671-1677 (2013). https://doi.org:10.1038/nn.3532

10 Kwon, S. E., Yang, H., Minamisawa, G. & O'Connor, D. H. Sensory and decision-related activity propagate in a cortical feedback loop during touch perception. *Nature Neuroscience* **19**, 1243-1249 (2016). https://doi.org:10.1038/nn.4356

11 Yang, H., Kwon, S. E., Severson, K. S. & O'Connor, D. H. Origins of choice-related activity in mouse somatosensory cortex. *Nature Neuroscience* **19**, 127-134 (2016). https://doi.org:10.1038/nn.4183

12 Buetfering, C. *et al.* Behaviorally relevant decision coding in primary somatosensory cortex neurons. *Nature Neuroscience* **25**, 1225-1236 (2022). https://doi.org:10.1038/s41593-022-01151-0

13 Gardères, P.-M. *et al.* Coexistence of state, choice, and sensory integration coding in barrel cortex LII/III. *Nature Communications* **15**, 4782 (2024). https://doi.org:10.1038/s41467-024-49129-9

14 Sofroniew, N. J., Cohen, J. D., Lee, A. K. & Svoboda, K. Natural Whisker-Guided Behavior by Head-Fixed Mice in Tactile Virtual Reality. *The Journal of Neuroscience* **34**, 9537-9550 (2014). https://doi.org:10.1523/jneurosci.0712-14.2014

15 Sofroniew, N. J., Vlasov, Y. A., Hires, S. A., Freeman, J. & Svoboda, K. Neural coding in barrel cortex during whisker-guided locomotion. *eLife* **4**, e12559 (2015). https://doi.org:10.7554/eLife.12559

16 Armstrong, A. G. & Vlasov, Y. A. Perceptual decision making during whisker guided navigation causally depends on a single cortical barrel column. *bioArxiv* **2025.02.17.638764** (2025). https://doi.org:10.1101/2025.02.17.638764

17 Wong, K.-F. & Wang, X.-J. A Recurrent Network Mechanism of Time Integration in Perceptual Decisions. *The Journal of Neuroscience* **26**, 1314 (2006). https://doi.org:10.1523/JNEUROSCI.3733-05.2006
18 Wang, X.-J. Probabilistic Decision Making by Slow Reverberation in Cortical Circuits. *Neuron* **36**, 955-968 (2002). https://doi.org:10.1016/S0896-6273(02)01092-9
19 Romo, R., Hernández, A., Zainos, A., Lemus, L. & Brody, C. D. Neuronal correlates of decision-making in secondary somatosensory cortex. *Nature Neuroscience* **5**, 1217-1225 (2002). https://doi.org:10.1038/nn950
20 Kleinfeld, D., Ahissar, E. & Diamond, M. E. Active sensation: insights from the rodent vibrissa sensorimotor system. *Current Opinion in Neurobiology* **16**, 435-444 (2006). https://doi.org:10.1016/j.conb.2006.06.009
21 Fassihi, A., Akrami, A., Pulecchi, F., Schönfelder, V. & Diamond, M. E. Transformation of Perception from Sensory to Motor Cortex. *Current Biology* **27**, 1585-1596.e1586 (2017). https://doi.org:10.1016/j.cub.2017.05.011
22 Chen, J. L., Carta, S., Soldado-Magraner, J., Schneider, B. L. & Helmchen, F. Behaviour-dependent recruitment of long-range projection neurons in somatosensory cortex. *Nature* **499**, 336-340 (2013). https://doi.org:10.1038/nature12236
23 Helmchen, F., Gilad, A. & Chen, J. L. Neocortical Dynamics During Whisker-Based Sensory Discrimination in Head-Restrained Mice. *Neuroscience* **368**, 57-69 (2018). https://doi.org:10.1016/j.neuroscience.2017.09.003
24 Guo, Zengcai V. *et al.* Flow of Cortical Activity Underlying a Tactile Decision in Mice. *Neuron* **81**, 179-194 (2014). https://doi.org:10.1016/j.neuron.2013.10.020
25 Li, N., Daie, K., Svoboda, K. & Druckmann, S. Robust neuronal dynamics in premotor cortex during motor planning. *Nature* **532**, 459-464 (2016). https://doi.org:10.1038/nature17643
26 Inagaki, H. K., Inagaki, M., Romani, S. & Svoboda, K. Low-Dimensional and Monotonic Preparatory Activity in Mouse Anterior Lateral Motor Cortex. *The Journal of Neuroscience* **38**, 4163-4185 (2018). https://doi.org:10.1523/jneurosci.3152-17.2018
27 Feldmeyer, D. *et al.* Barrel cortex function. *Progress in Neurobiology* **103**, 3-27 (2013). https://doi.org:10.1016/j.pneurobio.2012.11.002
28 von Heimendahl, M., Itskov, P. M., Arabzadeh, E. & Diamond, M. E. Neuronal Activity in Rat Barrel Cortex Underlying Texture Discrimination. *PLOS Biology* **5**, e305 (2007). https://doi.org:10.1371/journal.pbio.0050305
29 Colins Rodriguez, A., Loft, M. S. E., Schiessl, I., Maravall, M. & Petersen, R. S. Sensory adaptation in the barrel cortex during active sensation in the behaving mouse. *Scientific Reports* **14**, 21588 (2024). https://doi.org:10.1038/s41598-024-70524-1
30 Oesch, L. T., Ryan, M. B. & Churchland, A. K. From innate to instructed: A new look at perceptual decision-making. *Current Opinion in Neurobiology* **86**, 102871 (2024). https://doi.org:10.1016/j.conb.2024.102871
31 Steinmetz, P. N. *et al.* Attention modulates synchronized neuronal firing in primate somatosensory cortex. *Nature* **404**, 187-190 (2000). https://doi.org:10.1038/35004588
32 Engel, A. K., Fries, P. & Singer, W. Dynamic predictions: Oscillations and synchrony in top–down processing. *Nature Reviews Neuroscience* **2**, 704-716 (2001). https://doi.org:10.1038/35094565
33 Gilbert, C. D. & Li, W. Top-down influences on visual processing. *Nature Reviews Neuroscience* **14**, 350-363 (2013). https://doi.org:10.1038/nrn3476
34 Salinas, E. & Sejnowski, T. J. Correlated neuronal activity and the flow of neural information. *Nature Reviews Neuroscience* **2**, 539-550 (2001).

https://doi.org:10.1038/35086012
35 Pesaran, B., Pezaris, J. S., Sahani, M., Mitra, P. P. & Andersen, R. A. Temporal structure in neuronal activity during working memory in macaque parietal cortex. *Nature Neuroscience* **5**, 805-811 (2002). https://doi.org:10.1038/nn890
36 Bellardita, C. & Kiehn, O. Phenotypic Characterization of Speed-Associated Gait Changes in Mice Reveals Modular Organization of Locomotor Networks. *Current Biology* **25**, 1426-1436 (2015). https://doi.org:10.1016/j.cub.2015.04.005
37 Pillow, J. W. *et al.* Spatio-temporal correlations and visual signalling in a complete neuronal population. *Nature* **454**, 995-999 (2008). https://doi.org:10.1038/nature07140
38 Stringer, C. *et al.* Spontaneous behaviors drive multidimensional, brainwide activity. *Science* **364**, eaav7893 (2019). https://doi.org:10.1126/science.aav7893
39 Keller, Georg B., Bonhoeffer, T. & Hübener, M. Sensorimotor Mismatch Signals in Primary Visual Cortex of the Behaving Mouse. *Neuron* **74**, 809-815 (2012). https://doi.org:10.1016/j.neuron.2012.03.040
40 Musall, S. *et al.* Tactile frequency discrimination is enhanced by circumventing neocortical adaptation. *Nature Neuroscience* **17**, 1567-1573 (2014). https://doi.org:10.1038/nn.3821
41 Staiger, J. F. & Petersen, C. C. H. Neuronal Circuits in Barrel Cortex for Whisker Sensory Perception. *Physiological Reviews* **101**, 353-415 (2020). https://doi.org:10.1152/physrev.00019.2019
42 Cunningham, J. P. & Yu, B. M. Dimensionality reduction for large-scale neural recordings. *Nature Neuroscience* **17**, 1500-1509 (2014). https://doi.org:10.1038/nn.3776
43 Churchland, M. M. *et al.* Stimulus onset quenches neural variability: a widespread cortical phenomenon. *Nature Neuroscience* **13**, 369-378 (2010). https://doi.org:10.1038/nn.2501
44 Ganguli, S. *et al.* One-Dimensional Dynamics of Attention and Decision Making in LIP. *Neuron* **58**, 15-25 (2008). https://doi.org:10.1016/j.neuron.2008.01.038
45 Sato, T. & Schall, J. D. Pre-excitatory pause in frontal eye field responses. *Experimental Brain Research* **139**, 53-58 (2001). https://doi.org:10.1007/s002210100750
46 Shinn, M., Lee, D., Murray, J. D. & Seo, H. Transient neuronal suppression for exploitation of new sensory evidence. *Nature Communications* **13**, 23 (2022). https://doi.org:10.1038/s41467-021-27697-4
47 Shinn, M., Lam, N. H. & Murray, J. D. A flexible framework for simulating and fitting generalized drift-diffusion models. *eLife* **9**, e56938 (2020). https://doi.org:10.7554/eLife.56938
48 Stine, G. M., Trautmann, E. M., Jeurissen, D. & Shadlen, M. N. A neural mechanism for terminating decisions. *Neuron* **111**, 2601-2613.e2605 (2023). https://doi.org:10.1016/j.neuron.2023.05.028
49 Churchland, A. K. *et al.* Variance as a Signature of Neural Computations during Decision Making. *Neuron* **69**, 818-831 (2011). https://doi.org:10.1016/j.neuron.2010.12.037
50 Horwitz, G. D. & Newsome, W. T. Target Selection for Saccadic Eye Movements: Prelude Activity in the Superior Colliculus During a Direction-Discrimination Task. *Journal of Neurophysiology* **86**, 2543-2558 (2001). https://doi.org:10.1152/jn.2001.86.5.2543
51 Bollimunta, A., Totten, D. & Ditterich, J. Neural Dynamics of Choice: Single-Trial Analysis of Decision-Related Activity in Parietal Cortex. *The Journal of Neuroscience* **32**, 12684-12701 (2012). https://doi.org:10.1523/jneurosci.5752-11.2012
52 Falkner, A. L., Krishna, B. S. & Goldberg, M. E. Surround Suppression Sharpens the Priority Map in the Lateral Intraparietal Area. *The Journal of Neuroscience* **30**, 12787-12797 (2010). https://doi.org:10.1523/jneurosci.2327-10.2010
53 Derdikman, D., Hildesheim, R., Ahissar, E., Arieli, A. & Grinvald, A. Imaging

Spatiotemporal Dynamics of Surround Inhibition in the Barrels Somatosensory Cortex. *The Journal of Neuroscience* **23**, 3100 (2003). https://doi.org:10.1523/JNEUROSCI.23-08-03100.2003

54 Adesnik, H. & Scanziani, M. Lateral competition for cortical space by layer-specific horizontal circuits. *Nature* **464**, 1155-1160 (2010). https://doi.org:10.1038/nature08935

55 Theyel, B. B., Llano, D. A. & Sherman, S. M. The corticothalamocortical circuit drives higher-order cortex in the mouse. *Nature Neuroscience* **13**, 84-88 (2010). https://doi.org:10.1038/nn.2449

56 Mo, C., McKinnon, C. & Murray Sherman, S. A transthalamic pathway crucial for perception. *Nature Communications* **15**, 6300 (2024). https://doi.org:10.1038/s41467-024-50163-w

57 Papale, A. E. *et al.* Symmetry in Frontal But Not Motor and Somatosensory Cortical Projections. *The Journal of Neuroscience* **44**, e1195232024 (2024). https://doi.org:10.1523/JNEUROSCI.1195-23.2024

58 Aronoff, R. *et al.* Long-range connectivity of mouse primary somatosensory barrel cortex. *European Journal of Neuroscience* **31**, 2221-2233 (2010). https://doi.org:10.1111/j.1460-9568.2010.07264.x

59 Chakrabarti, S. & Schwarz, C. Cortical modulation of sensory flow during active touch in the rat whisker system. *Nature Communications* **9**, 3907 (2018). https://doi.org:10.1038/s41467-018-06200-6

60 McElvain, L. E. *et al.* Circuits in the Rodent Brainstem that Control Whisking in Concert with Other Orofacial Motor Actions. *Neuroscience* **368**, 152-170 (2018). https://doi.org:10.1016/j.neuroscience.2017.08.034

METHODS

Behavioral tactile virtual reality rig

The treadmill of **Fig.1A** is built around a hollow Styrofoam sphere (16-inches diameter) with walls custom-thinned to provide a total weight of less than 60g. The sphere is suspended on 7 ping-pong balls supported by 7 air-nozzles distributed around its bottom half[1-4] based on the design developed at the HHMI Janelia Research campus[5]. Controlled stimulus to animal whiskers is provided by a pair of motorized walls positioned at both sides of the snout. The animal movement in lateral (V_{lat}) and forward (V_{for}) directions is tracked at 500Hz by recording the sphere movement with two tracking cameras[6]. Turns were defined by a turn angle θ that was positive for left turns and negative for right.

$$\theta = \text{atan}\,(D_{lat}/D_{for}) \qquad \text{Eq.1}$$

where D_{for} and D_{lat} are lateral and forward displacements in a single cycle. This signal is used to provide positive feedback to the movement of the walls (V_{wall}):

$$V_{wall} = \gamma(V_{lat} \cdot \cos\theta - V_{for} \cdot \sin\theta) \qquad \text{Eq.2}$$

where γ is a calibrated feedback coefficient. When taken as negative it generates a positive closed-loop (CL) virtual reality (VR) that moves walls closer to the snout if the animal is moving closer to them and, therefore, encourage the animal to stay in the middle of the VR corridor.

The real time (RT) control and acquisition system is custom designed to power a FPGA CompactRIO (cRIO-9045, NI) with 32 channel analog voltage input module (NI 9205) to read sphere velocities, 4 channel analog output module (NI-9263) to operate mechanical walls, and 32 channel TTL input/output (NI-9403) to provide synchronization to video cameras and other equipment. The module is operated via LabVIEW RT Module (NI) by the custom designed LabVIEW acquisition and control program[4] that has Master/Slave architecture. The program operates several parallel processes that need to run simultaneously and continuously but at different rates. The master process runs in a loop at 30MHz and provides RT analog acquisition and control data to the rig. The master loop controls several slave loops and communicates with them using messaging architectures. One of the slave loops buffers recorded data and logs the data to disk at its own much slower pace. As a result, the acquisition and control experimental protocol executed in the master loop can run continuously without interruptions with virtually no inter-trial interval. Another slave loop is designed to provide a graphical user interface (GUI) that allows the user to observe data on the screen such as overlaid trial trajectories of the animal and to change parameters for each trial session if needed. Control signals generated in the master loop are directed to synchronize 3 high-speed cameras (**Fig.1A**) to acquire videos of whiskers and paws, as well as to synchronize behavioral recordings with electrophysiological recordings, optogenetic stimulation, and provide water rewards to the motorized licking port if needed.

The VR rig is enclosed in a light-tight box with fine copper mesh on the inside to provide shielding from ambient light and from EM interference. Constant hissing from air-nozzles provides stationary background acoustic white noise that masks all other ambient noises in the room. The surface of the Styrofoam sphere is coated with permanent water-resistive protective coating using low-odor latex aerosol (Krylon 7120) to enable the sphere to be cleaned between each animal thus minimizing olfactory cues. Therefore, the only sensory cues left for animals to use for navigation in the VR are whiskers palpating the motorized walls.

Animal preparation

This study is based on data from 19 mice of both sexes aged between P65 and P112 (**SI Table.1**). To ease identification of principal barrel and enable optogenetic tagging, the transgenic Scnn1a-TG3-Cre (Jackson:009613) line was crossed with the Ai32 line (Jackson: 012569), producing strong co-expression of the yellow fluorescent protein (YFP) and Channelrhodopsin-2 (ChR2H134R-EYFP) in ~85% of layer 4 excitatory neurons[7] in the primary somatosensory cortex (**Fig.1F**).

All procedures were in accordance with protocols approved by the UIUC Institutional Animal Care and Use Committee. Animals were kept on a reverse 12-hour light/dark cycle in individual cages equipped with activity wheels (K3250 Fast-Trac, Bio-Serv) to encourage active behavior in-between experimental sessions. All experimental sessions were performed during the dark phase. Surgical

procedures were carried out aseptically while animals are anesthetized with isoflurane (2-4% in oxygen) before being injected subcutaneously with 5mg/kg carprofen. To prepare animals for behavioral and electrophysiological studies a custom-built titanium headbar (10mm x 2 mm)[8] was attached to the animal's skull to hold the animal's head. Orientation of the headbar is carefully adjusted with respect to Bregma and Lambda points on the animal skull to provide a repeatable coordinate system for electrophysiological multielectrode probe insertion. The central open area of the headbar (3mm x 2mm) exposes the skull directly above the primary somatosensory cortex for in-vivo visualization, targeted craniotomy, and precise probe insertion. This area is covered in optical grade clear cement for in-vivo fluorescence imaging. For experiments with electrophysiological recordings, a craniotomy (approximately 0.2 mm in diameter) is made through the back of the headbar, and a ground wire (2 mm long Pt/Ir ground wire, A-M Systems 776000) is implanted in the cerebellum and cemented on the headbar. Beginning the day following the surgery, subcutaneous Carprofen (5mg/kg) is administered for two days to reduce inflammation. To restrict sensory information flow, all but a pair of C2 whiskers are trimmed at the time the animal is placed on water deprivation. Trimming is performed daily afterwards to avoid other whiskers growing.

Following full and complete recovery from a previous surgery, the animal is placed on a water restriction schedule[8] in preparation for behavioral conditioning. Food is continuously available. Water is adjusted (approximately 1 ml per day) so that mice maintain more than 80% of free-drinking weight. When fully adjusted to the water restriction protocol (weight stabilized) a mouse is habituated to virtual reality treadmill of **Fig.1A** with head fixation starting with 15min during the first day. Using a large diameter sphere (16 inches) in our VR rig as well as tunable head fixation enables to closely mimic the posture observed during natural locomotion[9]. Sessions are extended over 3-4 days to last up to 1 hour. During this time a mouse is encouraged to run by administering water rewards (0.1ml) given only if the running speed exceeds 5cm/sec for a total of 1 ml. Typically (**SI Table.1**), on day 3 a mouse is fully acclimatized to the apparatus, actively runs 80% of the time at elevated speed above 10cm/s (21±4cm/s, mean ± s.d., **ED Fig.1A**) and consumes all the daily water ration during experiment. When running, they navigate the straight VR corridor using only a pair of C2 whiskers while minimizing the lateral displacement to less than ±1cm (**ED Fig.1B**).

Stereotaxic-less probe positioning on a principal whisker barrel

We aim for precise placement of microelectrode probe strategically into the principal whisker barrel and to align it perpendicular to cortical layers. We also aim to produce active behavior when the head-fixed animal is running fast on a treadmill navigating virtual turns for the whole duration of the electrophysiological recordings. This precludes the use of stereotaxic surgery for electrode insertion. Therefore, we developed a protocol for highly precise probe insertion when the animal is placed and head fixed in the VR rig.

The first step is to acquire a brain map of the somatosensory cortex generalized across many animals (**ED Fig.3D**). For that we used fluorescence top-down imaging (Olympus, MVX10) of the whole fixed brain harvested immediately after the final terminal experiment (**ED Fig.3C**). To match vasculature patterns with those observed in-vivo in the same animal (**ED Fig.3B**), mice were deeply anesthetized with 5% isoflurane then perfused with 0.1 M sodium phosphate buffer for just a short period of time to ensure that some blood remains in top arterioles on the brain surface. Resulting brain preparations not only show characteristic contours of primary visual cortex (V1), the barrel cortex (wS1), as well as characteristic shapes of lower jaw (LJ) and hindpaw (HP) somatosensory areas (**ED Fig.3C**), but also in some cases show identifiable locations of main barrels across main B, C, and D rows (**Fig.1G**). Combining similar images from several animals, a generalized map is created with positions of individual barrels relative to the contours of V1 and S1 areas (**ED Fig.3D**).

Next, for a given mouse, to map in-vivo the location of the target C2 barrel without the use of stereotaxic apparatus, the mouse is anesthetized with isoflurane (2-4% in oxygen) and the brain is imaged in-vivo (**ED Fig.3A**) through the central open area of the headbar that exposes the skull directly above the primary somatosensory cortex (nominal coordinates for C2 barrel 2.0mm AP, 3.4mm ML). The YFP expression in L4 excitatory cells in the primary somatosensory and visual cortices is strong enough to identify contours of V1, wS1, LJ and HP areas as well as characteristic vasculature patterns

through the skull (**Fig.1F, ED Fig.3B**), and to align them to previously acquired cortical map (**ED Fig.3D**). This procedure allows us to mark the location of the C2 barrel with respect to the headbar with localization precision as high as ±0.1mm as confirmed by subsequent histological mapping (see below) (**Fig.1H**).

Targeted craniotomy

On the morning of the final terminal experimental session, mice are briefly anesthetized with isoflurane (2-4% in oxygen) and are placed in a head-fixation surgery apparatus closely mimicking head-fixation setup in the VR rig. Fluorescence imaging is performed with overhead stereo microscope (MZ12.5, Leica) equipped with fluorescence adaptor (Quad Fluorescence System, Kramer Scientific). Brain map with location of targeted C2 principal whisker barrel generated during in-vivo fluorescent imaging (**ED Fig.3B, D**) is compared with microscope imaging to check the marked location of targeted craniotomy on the skull surface. Using a microdrill with 0.002" burrs (Fine Science Tools, Canada), the optical cement and the skull are carefully thinned while the surface is cooled down using sterile artificial cerebrospinal fluid (ACSF). A small craniotomy of < 300µm diameter is opened while the dura remained intact. The craniotomy site is then imaged both in a white light and with fluorescence filters to visualize a barrel field and a vasculature pattern and to produce a final map for probe implantation. The craniotomy site is covered with a silicone elastomer plug (World Precision Instruments, USA). The whole procedure typically lasts less than 30 mins and mice are returned to home-cage for recovery for at least 2 hours. Typically, mice are fully recovered within 20 mins and frequently running on activity wheels.

Electrophysiological recordings

For extracellular electrophysiological recordings we used either (**SI Table 1**) a 64-channel linear shank silicon probes (Cambridge NeuroTech, UK) connected to Intan head stage (Intan, USA) or Neuropixels (1.0, Imec) electrode arrays with 383 recoding sites selectable from a total of 960, connected to custom PXIe acquisition module (Neuropixels, Imec). The acquisition board (OEPS-9030, OpenEphys) and Open Ephys GUI were used to demultiplex and visualize recorded voltages. The TTL signals from the RT LabVIEW acquisition program were used to synchronize recordings in real time with behavioral sessions. Probes were mounted to a custom 3D-printed holder and attached to a steel rod held by a robotic micromanipulator (MPM System, New Scale Technologies) at 38 degrees around the animal head AP axis to ensure shank was perpendicular to cortical layers in the C2 barrel column. The inner surface of the probes was painted with DiI (V22888, ThermoFisher) for post hoc probe track visualization during histology.

Once mice are placed and head-fixed in the VR rig they almost immediately start to run. To direct animals, the behavioral session starts right away with closed loop CL straight run. The animal skull with a craniotomy site mapped previously is observed with overhead stereo microscope (MZ12.5, Leica), plug is removed, and a silicon probe is positioned over the C2 principal whisker barrel and slowly implanted at constant speed (50-200µm/min) to a full cortical depth of 1mm. Once inserted, the probe was left to settle for at least 5 minutes prior to the start of the main behavioral session. For most sessions the craniotomy site was covered with a saline sterile ACSF bath. In some experiments saline-based agar was used covered with silicone oil to prevent drying.

Optogenetic and histological verification of electrode position

At the end of every electrophysiological session an in-vivo optogenetic stimulation of layer 4 was performed using fiber-pigtailed 473nm laser light (10 Hz with 2 ms pulses, 1 mW peak) focused on the craniotomy area to obtain current source density (CSD) traces. Characteristic negative sink at short time scale after the optical pulse is used to identify the position of layer 4 (**Fig.1I**).

In sessions where 64-channels probes were used (**SI Table 1**), small electrolytic lesions were made using the lowest electrode of the silicon probe to ease identification of the electrode depth in histology (arrow in **Fig.1H** and **ED Fig.3E, F**). For that purpose, corresponding pins in a head stage board were connected via external wire to a constant current isolated stimulator (DS3, Digitimer). Then 10µA of current was sent through the wire to the lesion electrode for 500 ms while the head stage was disconnected.

Immediately after the end of final terminal experiment, mice were deeply anesthetized with 5% isoflurane then partially perfused to enable vasculature to be visible. Harvested brains removed from the skull were immediately imaged with top-down fluorescence microscopy that enables matching of postmortem vasculature patterns (**Fig.1G** and **ED Fig.3C**) with those observed in-vivo (**Fig.1F** and **ED Fig.3B**) and to identify the DiI-marked entry point of the probe (**Fig.1G**) with the barrel field map (**ED Fig.3D**) using image overlay alignment (Photoshop, Adobe Suite). The brains were then sectioned into 70-µm-thick coronal sections (VT1200S, Leica) to allow for visualization of DiI-stained probe tracks, electrolytic lesions (**ED Fig.3E**), and identification of cortical layers (**ED Fig.3F**). Strong YFP expression in Layer 4 clearly identifies individual barrels (**ED Fig.3F**). Dense projections to layer 2/3 terminate at the border with layer 1 that ease its identification. Layer 6 has the lowest YFP intensity (**ED Fig.3G**) enabling further identification of the border between layer 5 and layer 6. Expression is not uniform across layer 5 with stronger expression at its bottom that is assigned to the boundary between layer 5A and 5B (**ED Fig.3G**). Combination of YFP intensity distribution, lesion location, the location of DiI probe traces, as well as the CSD analysis were critical for localization of the laminar position of the recording electrodes (**Fig.1G**). Each electrode was then assigned a depth value that is later used to assign recorded units to cortical depths and layers within a given barrel column (**Fig.4C, D**).

We also registered electrodes and units to the Allen Institute Common Coordinate Framework (CCFv3)[10] by marking 20 registration points in consecutive coronal slices. Fluorescent probe tracks were manually labelled and used to translate the probe track positions into the CCFv3 coordinate space. We found, however, that manual reconstruction of electrode positions with respect to positions of L4 barrels and cortical layers individually for each animal using methodology described above was more precise than provided by a global CCFv3 mapping that does not define individual barrels. Therefore for our analysis we used our manual reconstructions of a probe position for the principal and neighbor barrels as shown in **Fig.4C,D**.

Spike sorting and unit filtering

The pipeline for spike sorting and filtering is shown in **ED Fig.2A**. The recorded electrophysiology data were automatically spike sorted using Kilosort3 (https://github.com/cortex-lab/Kilosort). The sorted datasets were passed through the Ecephys code for spike sorting pipeline (Allen Institute for Brain Science, Ecephys package, https://github.com/AllenInstitute/ecephys_spike_sorting) using functions kilosort_postprocessing, mean_waveforms and quality_metrics. Quality metrics to filter out putative single units (**ED Fig.2B**) were defined by Ecephys default values as amplitude cutoff ≤0.1mV, ISI violations ≤0.5, presence ratio ≥0.90. We also used waveform amplitude, signal to noise ratio, waveform duration, waveform spread, isolation distance, nearest neighbor' hit rate, and mean firing rate to further filter units. Finally, the waveforms were manually curated with the Phy GUI (https://github.com/kwikteam/phy). During manual curation, each unit was inspected and units with artefactual waveforms and putative double-counted spikes were discarded. The finalized 634 units (**ED Fig.2C**) were classified as fast spiking (FS, putative inhibitory) and regular spiking (RS, putative excitatory) based on their waveform duration using 0.4ms as a threshold (**ED Fig.2D**). Electrode position mapping for individual animals enables assignment of units to cortical depth based on the location of electrode with maximum voltage and to cortical layers (**ED Fig.2E**). Distribution of all units across layers (**ED Fig.2F**) reveals a typical bias towards layers 5A and 5B with less contribution from layer 2/3, mostly dictated by their sparser spiking and lower spike amplitudes.

Spiking data for all filtered units for each animal for the final terminal session are packaged together with behavioral data into Neurodata Without Borders files for further analysis (NWB2.0, https://github.com/NeurodataWithoutBorders/nwb-schema).

Whisker tracking and reconstruction of whisker angle and curvature

High speed overhead video of the whisker (**Fig.2E**, **SI Video 1**) was captured simultaneously with the electrophysiology recordings using the overhead (cam1 in **Fig.1A**) 656 × 600 pixels camera at 1000–1000 fps (EoSens1, Mikrotron) equipped with a 0.36× telecentric lens that produced 25 mm × 23 mm field-of-view (Edmund Optics, no. 58-257). Video streams were digitized with a frame grabber (BitFlow Axion) controlled by StreamPix7 multicamera software (NorPix). To align videoframes to the master

clock with less than 1 ms jitter, a video system was triggered from the main RT LabVIEW acquisition program. The field of view (FOV) is adjusted (MC ControlTool, Mikrotron) to capture the full length of the C2 whisker as well as its bent shape when interacting with a wall. The whisker was illuminated by an overhead LED light source (ThorLabs M810L3) powered by DC power supply (Mean Well RS-15-24) and focused with 40 mm focal length aspheric condenser (Thorlabs, ACL5040U).

Whisker movement during interaction with the wall was tracked by extracting individual lossless frames for subsequent manual analysis or using automated tracking with SLEAP[11] model (**Fig.2F**). A skeleton of five points along the C2 whisker was manually identified for 50-100 frames for each video and used as the training dataset for the model. Once trained, the model was used to make inferences on all frames in the video using the Hungarian matching method. The angle of the whisker is defined as 0° when it is perpendicular to the mouse head AP axis. The first two tracking points along the whisker length in each frame were used to calculate the whisker angle. To extract whisker curvature from the tracking results, a Bezier quadratic was fit to the three points closest to the base of the whisker and the curvature was obtained via De Casteljau's algorithm.

Tracking of fore paws and hind paws and reconstruction of gait

Videos of hind paws and fore paws (**Fig.2G, SI Video1**) were captured using a pair of 659 × 494 pixels cameras at 50fps (Basler acA640) (cam2 and cam3 in **Fig.1A**) equipped with 16 mm lenses that produced 34 mm × 23 mm FOV. Cameras were positioned above the hind limbs and to the side of the front limbs and were triggered from the main RT LabVIEW acquisition program. The FOVs were illuminated by additional LED light sources.

Frame-by-frame manual inspection of the paw's videos (**SI Video1**) enabled reconstruction of the animal gait (**Fig.2H**, bottom) by recording the precise timings of when each paw is in contact with the sphere (**Fig.2G**). This reconstruction is confirmed by observation of characteristic periodic oscillations (**Fig.2H**, middle) in a derivative of the recorded traces of turn angle θ (or lateral acceleration). Characteristic coordinated sequence of diagonal LH-RF and RH-LF strides corresponds to trotting, the natural gait that animal is producing[9] to accommodate speeds faster than 20cm/s.

Data analysis

Spike rates for individual units and populations

To visualize firing rates for individual units, the spiking activity was binned at 0.005s and plotted as raster plots (**ED Fig.5A,B** and **ED Fig.10**, bottom) or averaged across all corresponding trials (**ED Fig.5C,D** and **ED Fig.10**, middle). The raster plots of population activity (**Fig.1J,K** and **ED Fig.4**) are combined from individual units z-scored trial-averaged spike rates. Population spike rates plots (**Fig.1L-K** and **ED Fig.4**) represent population-averaged spike rates normalized on the number of units recorded for a given animal. For comparison with DDM results (**Fig.3B** and **ED Fig.9**) or between animals (**Fig.4B-D**), the population spike rates are presented as normalized values with minimum and maximum spike rates normalized to 0 and 1, respectively.

Multiparameter GLM regression

To assess which variables contribute the most to the neural activity during closed-loop baseline straight running, we used a multi-parameter generalized linear-nonlinear Poisson model[12] (GLM). Pyhton code was used available publicly from https://github.com/pillowlab/GLMspiketraintutorial_python.

The spike trains during closed loop CL straight running trials were merged for all excitatory layer 4, 5A and 5B units. The same 3 second segment was used for 40 randomly selected CL trials. Spikes were split into 20ms time bins and smoothed using a Savitzky-Golay filter. A Hankel matrix was constructed for each of the 13 variables using 250 x 20ms time bins, for spike prediction. Spike triggered average (STA) was computed and visualized for each of the matrices to produce an unbiased estimator of the filter to be used and determine if any issues were encountered. We then computed a whitened STA; the maximum-likelihood estimator for the filter. Pre-whitening is a common method used to remove autocorrelations from residuals before GLM analysis of neural data. The whitened STA was used for

model fitting using the 'glmfit' python function with Poisson noise model and exponential link function. Spike predictions and subsequent quantification of performance were recorded for each regressor.
For regressions we used a set of simultaneously recorded parameters of whisking, gait, speed and direction. To correlate whisking motor actions that are known to strongly contribute to spiking activity[13-15], whisking phases and amplitudes were extracted from the tracked whisking angle using Hilbert transform. To correlate locomotion parameters, run angle derivative and times for RH and LH legs pushes were used. Together with speed parameters (forward and absolute speeds) as well as direction parameters (run angle and lateral speed) the pool accounted for 12 regressors. Although they do not form orthogonal basis as some of them depend on each other, however they cover different aspects of sensory input (whisking), locomotion (speed, gait) and motor action output (direction) (**Fig.2J**). Additionally, we included a feedback parameter V_{wall} defined by Eq.2 that appears to produce the highest contribution.

Dimensionality reduction

Analysis of intrinsic dimensionality of population activity is based on calculating principal components (PC) on the dataset and estimating the 90% of the data variance that can be explained by a minimal number of PC. The dimensionality reduction code following a standard PCA reduction method[16,17] is rewritten in Python and is used for analysis in **Fig.2I**. The spiking activity for each unit was taken in 100ms epochs across all trials of the same type, with mean rates calculated in 1ms time bins for each unit. A 2ms gaussian smoothing kernel was used and units with a firing rate <1Hz were removed. Subsequently, for each 100ms segment, a matrix of trial average spike rates was produced and used for PC analysis. The number of latent variables required to explain 90% of the variance was assigned as the dimensionality for that segment.

Fitting of drift diffusion models

Reaction times (RT) are extracted from lateral acceleration (or run angle derivative) as the largest peak in the time interval after the start of the turn trial (**Fig.2H**, middle). Such peaks are associated with characteristic push with RH or LH legs as observed from videography of the animal locomotion. These peaks are highly reproducible for hundreds of randomized left and right turn trials for all animals (**ED Fig.7** and **ED Fig.8**). We assigned a correct score to the turn if animal is achieving ±1cm clearance at t=1s from the trial start, otherwise the trial is marked as error. For an example animal in **Fig.2A** the success rate is reaching 95% (14 failed trajectories in red). Similar results are obtained for other animals (**ED Fig.6**). Corresponding distributions of correct and error RT are shown in **Fig.3B** and **ED Fig.9**. To fit the RT with different drift diffusion models we used a Python based pyDDM generalized drift diffusion model[18] (https://github.com/mwshinn/PyDDM).

Analysis of varCE

To calculate varCE and corCE we followed the method[19]. For each 10ms time bin the mean number of spikes for each unit $\overline{N}$ was calculated together with the total variance of the spike counts $s^2_{N_i}$ across all left turn trials. The total variance of this doubly stochastics process becomes a sum of two separate components[19]: point process variance (PPV) that is proportional to mean spike rates and variance of conditional expectation (varCE) that reflects the variance of rates.

$$varCE = s^2_{N_i} - \phi\overline{N}_i \qquad \text{Eq.3}$$

where the constant ϕ was estimated using the time bin that contains the lowest Fano factor that ensures the VarCE remains positive throughout the choice period. The PPV was defined as:

$$PPV = \langle \sigma^2_{N_i|\lambda_i} \rangle \qquad \text{Eq.4}$$

where N_i is the number of spikes in the bin and λ_i the firing rate.

For an example unit the total variance (**ED Fig.10A**, middle, red) follows the mean (**ED Fig.10A**, middle, blue) for epochs 1 and 2, that results in a Fano factor (**ED Fig.10A**, top, black) of 0.74±0.04 (mean ± s.d.). Total variance saturates midway through a strong increase of mean firing rate during ramping that results in a Fano factor dropping down to 0.29 at the peak of epoch 4 at t=0.23s and then slowly restores back in epoch 5. If all the total variance at t=0.23s is taken as coming from the PPV,

then constant ϕ can be taken as 0.29. The resulting varCE (**Fig. 3F**, red) exhibits a fast increase at the beginning of epoch 4 between t=0.12s and t=0.17s (**Fig. 3F**, up and down arrows) indicating accumulation of stochastic trial-by-trial diffusion noise[19,20].

To estimate varCE for the whole population, we estimated constant ϕ in a similar manner for each unit and the resulting population varCE is shown in **Fig.3H**. Population varCE is then a union of units varCE as shown in **Fig.3G**, blue curve. Strong variation of mean spike rates among units may affect the combined population varCE (**Fig.3I**). However, when several major outliers are taken out, the resulting population varCE shows a similar increase during choice period (**Fig.3G**, red curve). Another approach to prevent this variation among the units from contributing to the combined population variance, is to estimate the total variance using the residuals method[19,20]. Residuals were calculated on a trial-by-trial basis, for each unit individually where the mean spike count in each time bin was subtracted from actual spike count across all trials. The population varCE is calculated as a union of varCE for every unit across all trials calculated on residuals instead of raw spike rates (**Fig.3G**, black curve). In all approaches the population varCE exhibit strong increase between t=0.12s and t=0.18s (**Fig. 3G**, up and down arrows) consistent with accumulation of stochastic trial-by-trial diffusion noise[19,20].

Analysis of corCE

If trial-by-trial variance of spike rates is defined by a diffusion process, then the correlation between pairs of rates at different times during a trial, the CorCE, should increase in consecutive time bins indicating accumulation of noise during evidence accumulation[19,20]. Covariance of conditional expectation (corCE) was calculated on residuals, with a covariance matrix having non-diagonal terms that correspond to corCE while the matrix diagonal corresponds to VarCE

$$corCE = cov[\langle N_i|\lambda_i\rangle, \langle N_i|\lambda_i\rangle] \qquad \text{Eq.5}$$

where, N_i is the number of spikes in the bin and λ_i the firing rate.

Streak Index analysis

To analyze local spike count fluctuations we followed the method[21], that in contrast to the original approach[22], is calculating the SI for each individual trial and analyzes its distribution across trials that provides a single-trial measure. For that the spike counts from all layers combined in 8 successive 5 ms bins were obtained for each trial. The spike counts in each bin for each trial were compared with the corresponding median spike counts calculated across all trials. The symbol “1” was assigned to bins where the count was higher than the median and “0” was assigned to bins where the count was lower than the median. The resulting binary sequence across trials was used to create a ‘streak index plot’ (**ED Fig.10D**). Then we counted how often switching either from 0 to 1 or from 1 to 0 occurred in the resulting 8-digit string to obtain a streak index value for each trial, with the distribution shown in **Fig.3K**. The distribution is close to normal with close to zero mean (0.06±1.36, mean ± s.d., **Fig.3K**) that indicates gradual rather than step-like transition in each trial during ramping.

References

1 Cohen, J. D., Bolstad, M. & Lee, A. K. Experience-dependent shaping of hippocampal CA1 intracellular activity in novel and familiar environments. *eLife* **6**, e23040 (2017). https://doi.org:10.7554/eLife.23040

2 Sofroniew, N. J., Cohen, J. D., Lee, A. K. & Svoboda, K. Natural Whisker-Guided Behavior by Head-Fixed Mice in Tactile Virtual Reality. *The Journal of Neuroscience* **34**, 9537-9550 (2014). https://doi.org:10.1523/jneurosci.0712-14.2014

3 Sofroniew, N. J., Vlasov, Y. A., Hires, S. A., Freeman, J. & Svoboda, K. Neural coding in barrel cortex during whisker-guided locomotion. *eLife* **4**, e12559 (2015). https://doi.org:10.7554/eLife.12559

4 Armstrong, A. G. & Vlasov, Y. A. Perceptual decision making during whisker guided navigation causally depends on a single cortical barrel column. *bioArxiv* **2025.02.17.638764** (2025). https://doi.org:10.1101/2025.02.17.638764

5 Large spherical treadmill for rodents. *HHMI Janelia Research Campus* (2010). <https://www.janelia.org/open-science/large-spherical-treadmill-rodents>.

6 Seelig, J. D. *et al.* Two-photon calcium imaging from head-fixed Drosophila during optomotor walking behavior. *Nature Methods* **7**, 535-540 (2010). https://doi.org:10.1038/nmeth.1468

7 Madisen, L. *et al.* A toolbox of Cre-dependent optogenetic transgenic mice for light-induced activation and silencing. *Nature Neuroscience* **15**, 793-802 (2012). https://doi.org:10.1038/nn.3078

8 Guo, Z. V. *et al.* Procedures for behavioral experiments in head-fixed mice. *PLoS One* **9**, e88678 (2014). https://doi.org:10.1371/journal.pone.0088678

9 Bellardita, C. & Kiehn, O. Phenotypic Characterization of Speed-Associated Gait Changes in Mice Reveals Modular Organization of Locomotor Networks. *Current Biology* **25**, 1426-1436 (2015). https://doi.org:10.1016/j.cub.2015.04.005

10 Wang, Q. *et al.* The Allen Mouse Brain Common Coordinate Framework: A 3D Reference Atlas. *Cell* **181**, 936-953.e920 (2020). https://doi.org:10.1016/j.cell.2020.04.007

11 Pereira, T. D. *et al.* SLEAP: A deep learning system for multi-animal pose tracking. *Nature Methods* **19**, 486-495 (2022). https://doi.org:10.1038/s41592-022-01426-1

12 Pillow, J. W. *et al.* Spatio-temporal correlations and visual signalling in a complete neuronal population. *Nature* **454**, 995-999 (2008). https://doi.org:10.1038/nature07140

13 Berg, R. W. & Kleinfeld, D. Rhythmic Whisking by Rat: Retraction as Well as Protraction of the Vibrissae Is Under Active Muscular Control. *Journal of Neurophysiology* **89**, 104-117 (2003). https://doi.org:10.1152/jn.00600.2002

14 Kleinfeld, D., Ahissar, E. & Diamond, M. E. Active sensation: insights from the rodent vibrissa sensorimotor system. *Current Opinion in Neurobiology* **16**, 435-444 (2006). https://doi.org:10.1016/j.conb.2006.06.009

15 McElvain, L. E. *et al.* Circuits in the Rodent Brainstem that Control Whisking in Concert with Other Orofacial Motor Actions. *Neuroscience* **368**, 152-170 (2018). https://doi.org:10.1016/j.neuroscience.2017.08.034

16 Cowley, B. R. *et al.* DataHigh: graphical user interface for visualizing and interacting with high-dimensional neural activity. *Journal of Neural Engineering* **10**, 066012 (2013). https://doi.org:10.1088/1741-2560/10/6/066012

17 Cunningham, J. P. & Yu, B. M. Dimensionality reduction for large-scale neural recordings. *Nature Neuroscience* **17**, 1500-1509 (2014). https://doi.org:10.1038/nn.3776

18 Shinn, M., Lam, N. H. & Murray, J. D. A flexible framework for simulating and fitting generalized drift-diffusion models. *eLife* **9**, e56938 (2020). https://doi.org:10.7554/eLife.56938

19 Churchland, A. K. *et al.* Variance as a Signature of Neural Computations during Decision

Making. *Neuron* **69**, 818-831 (2011). https://doi.org:10.1016/j.neuron.2010.12.037

20 de Lafuente, V., Jazayeri, M. & Shadlen, M. N. Representation of Accumulating Evidence for a Decision in Two Parietal Areas. *The Journal of Neuroscience* **35**, 4306-4318 (2015). https://doi.org:10.1523/jneurosci.2451-14.2015

21 Bollimunta, A., Totten, D. & Ditterich, J. Neural Dynamics of Choice: Single-Trial Analysis of Decision-Related Activity in Parietal Cortex. *The Journal of Neuroscience* **32**, 12684-12701 (2012). https://doi.org:10.1523/jneurosci.5752-11.2012

22 Horwitz, G. D. & Newsome, W. T. Target Selection for Saccadic Eye Movements: Prelude Activity in the Superior Colliculus During a Direction-Discrimination Task. *Journal of Neurophysiology* **86**, 2543-2558 (2001). https://doi.org:10.1152/jn.2001.86.5.2543

EXTENDED DATA

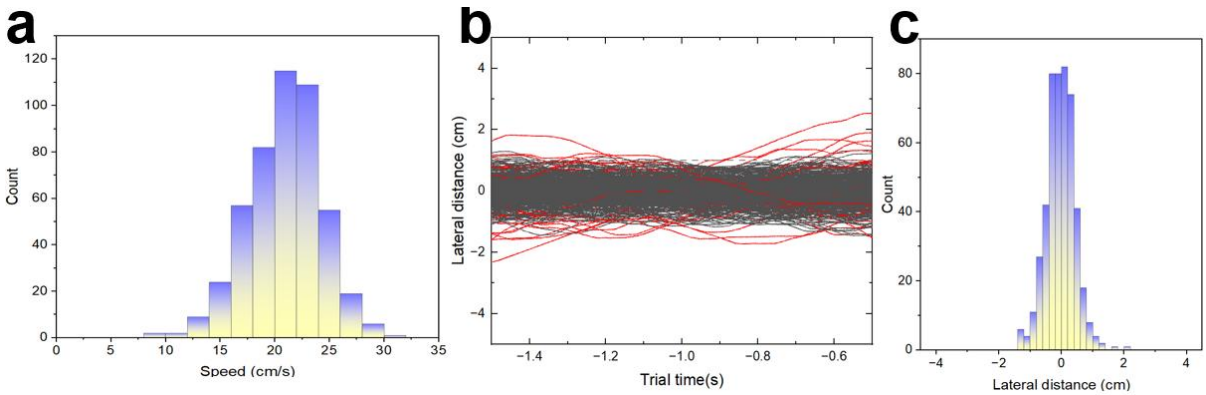

Figure 1. Closed loop straight run.
A) Histogram of a mouse (animal 503) absolute speed during 1.5 hour 481 trials experiment in Fig.3A.
B) Mouse trajectories for a closed-loop straight run portion of 481 trials. Red trajectories correspond to deviation of lateral distance larger than 1cm.
C) Histogram of lateral distance at t = -1s trial time.

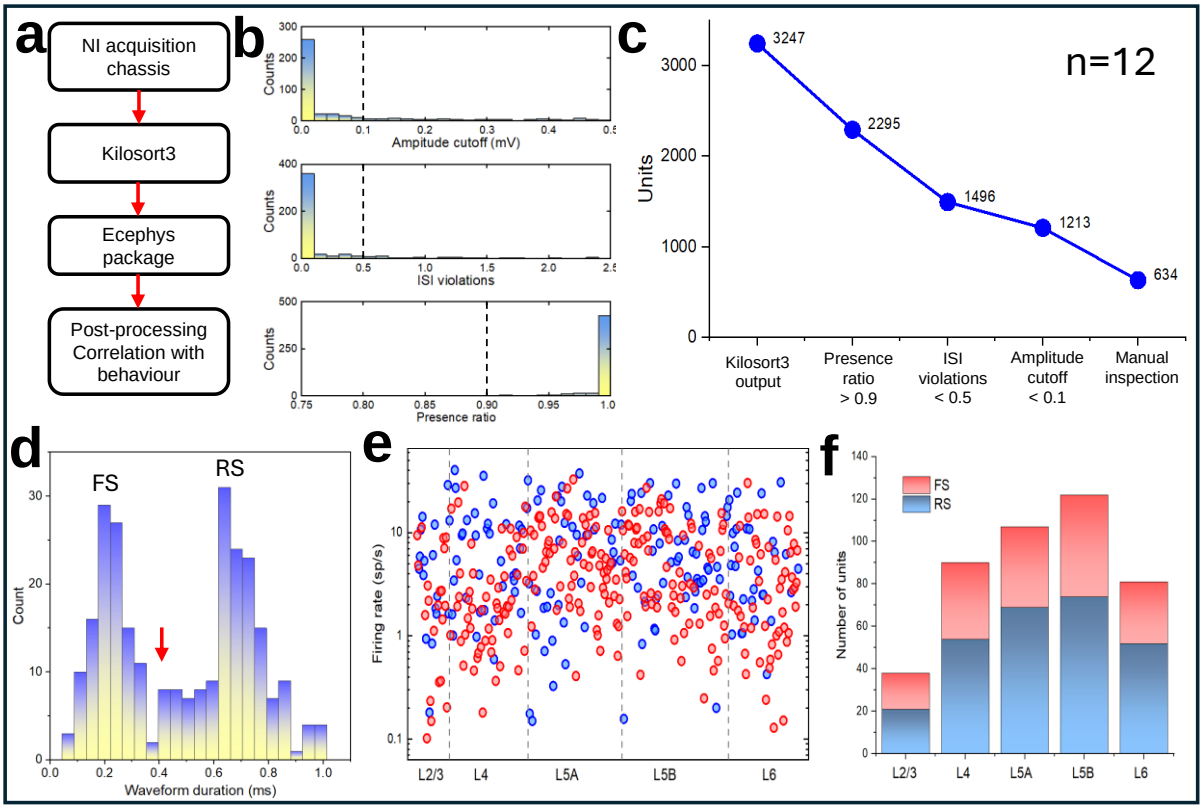

Figure 2. Electrophysiology pipeline.

A) Block-diagram of spike-sorting and filtering pipeline.

B) Three major filters to ensure the spike sorting quality: amplitude cutoff (top), ISI violations (middle, and presence ratio (bottom).

C) Filtered number of units recorded from n=12 animals in the principal whisker C2 barrel (blue) and neighboring barrels (red). See Table S1 for details.

D) Histogram of sorted spikes waveform duration. Cutoff at 0.4ms was used to classify RS and FS units.

E) Trial averaged spiking rates for all sorted units ordered by cortical depth and assigned to cortical layers. Red and blue dots correspond to FS and RS units respectively.

F) Distribution of sorted units across cortical layers for FS (red) and RS (blue) units.

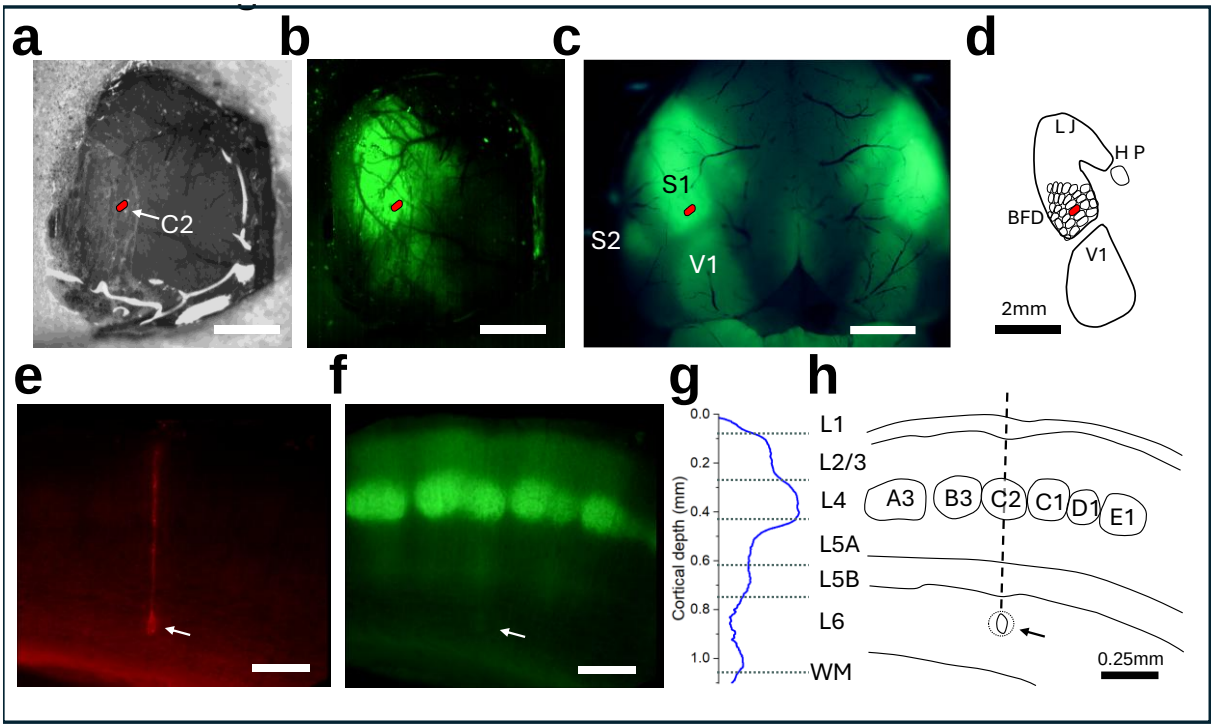

Figure 3. Targeting of C2 barrel and histological verification of probe position.

A) In-vivo top-down microscope view of the cranial window after surgery at white light illumination. Red oval corresponds to identified position of the principal whisker C2 barrel.

B) Same as in A) but with fluorescence filter. Green fluorescence from YFP expressed through the barrel cortex is used as a guide for identifying the location of the principal whisker barrel.

C) Fluorescent microscope image of the brain harvested and partially perfused immediately following the behavior experiment. Partially perfused vasculature pattern is used as a guide to align in-vivo and ex-vivo barrel maps.

D) Map of the barrel cortex with positions of individual barrels including the principal whisker C2 (red oval) derived from C) and Fig.1G.

E) Fluorescence micrographs of a coronal slice though a principal whisker barrel column (animal 489) taken with a green filter showing YFP expressed in layer 4 with projections to layer 2/3 above and layer 5B below. Arrow indicates location of a microlesion produced by the first electrode to identify the location of the probe tip.

F) Same as in E) but taken with a red filter showing the probe DiI track. Arrow indicates location of a microlesion performed with the first electrode to identify the location of the probe tip.

G) Intensity of YFP measured across the column (log scale).

H) Map of cortical layers and L4 barrels reconstructed from E) and F).

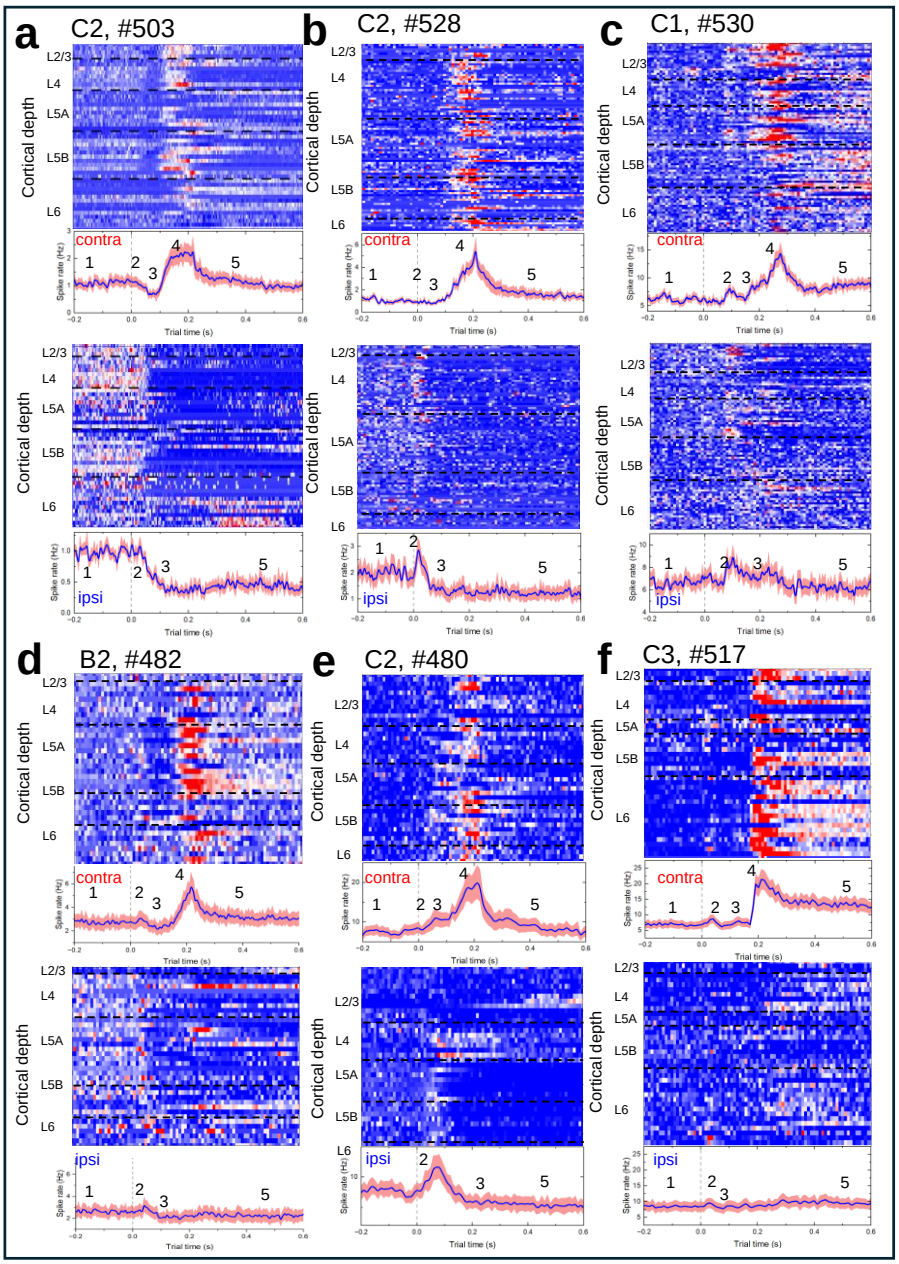

Figure 4. Population neural activity in principal whisker barrel column exhibits strong, staged, and synchronous modulation during decision-making process.

A) Animal 503. Recording from C2 principal barrel column. **Top panel:** Trial-averaged z-scored spiking activity units across the principal barrel column for OL_L left turns. Units are ordered by cortical depth and assigned to cortical layers. **Second panel**: Population-averaged spike rate for data in A) for OL_L left turns. Numbers correspond to modulation epochs 1 through 5. Blue curve is population mean. Red shadows correspond to mean ± s.e.m. **Third panel**: Same as Top for OL_R right turns. **Bottom panel**: Same as in Second for data in Third panel for OL_R right turns. 48 units, 305 OL_L trials, 304 OL_R.

B) Animal 528. Recording from C2 principal barrel column. 89 units, 95 OL_L trials, 95 OL_R.

C) Animal 530. Recording from C1 neighbor barrel column. 113 units, 402 OL_L trials, 403 OL_R.

D) Animal 482. Recording from B2 neighbor barrel column. 38 units, 350 OL_L trials, 350 OL_R.

E) Animal 480. Recording from C2 principal barrel column. 42 units, 185 OL_L trials, 190 OL_R.

F) Animal 517. Recording from C3 neighbor barrel column. 42 units, 270 OL_L trials, 268 OL_R.

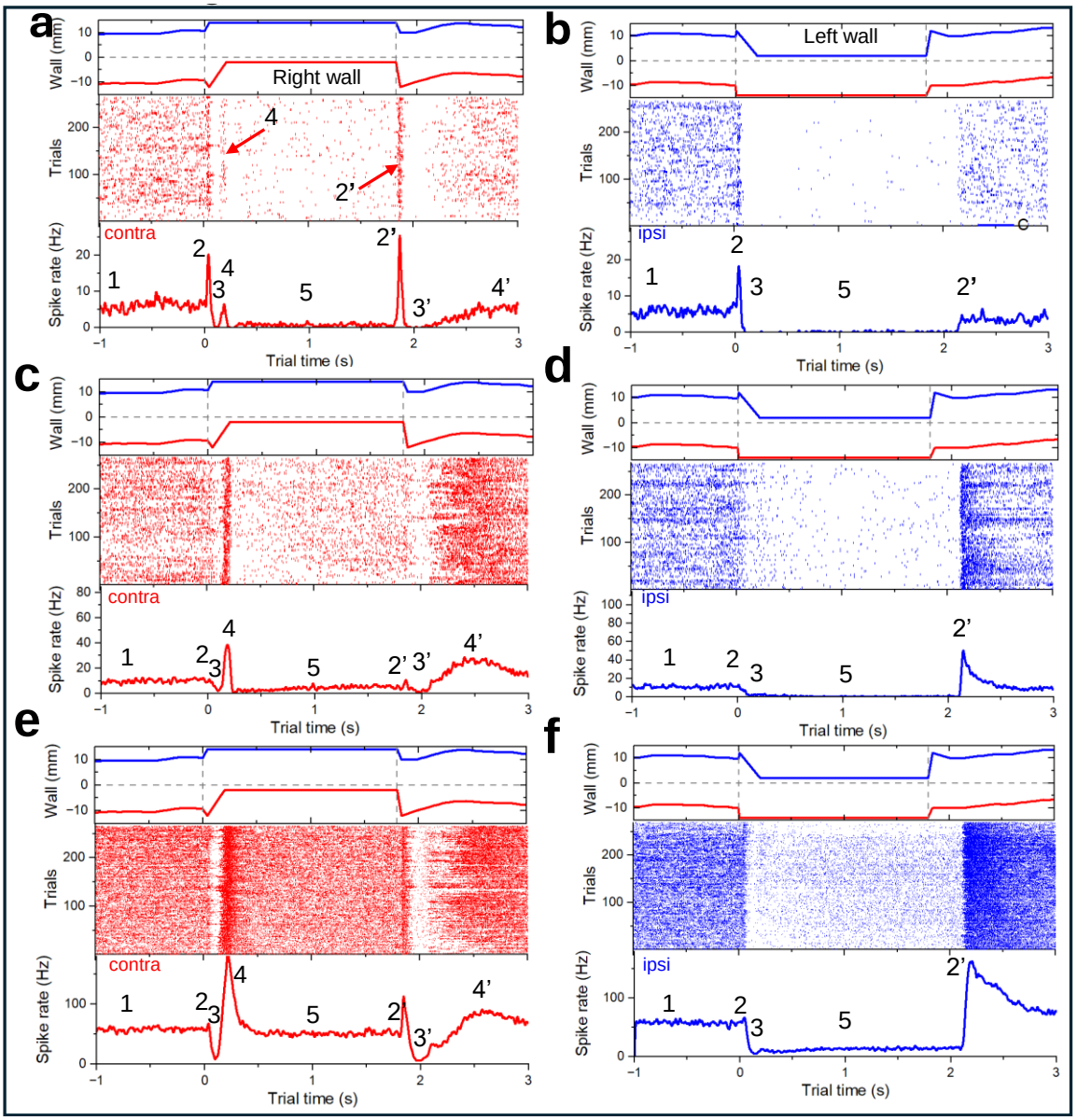

Figure 5. Single unit neural activity in principal whisker barrel column exhibits strong, staged, and synchronous modulation during decision-making process.

A) Top panel: Right (red) and left (blue) wall positions during the OL_L turn experiment. Middle panel: spiking raster plot of a unit (animal 489, unit 489085, FS, layer 4) recorded during 266 randomized left turns. Bottom panel: Trial-averaged spike rate of a single unit.

B) Top panel: Right (red) and left (blue) wall positions during the OL_R turn experiment. Middle panel: spiking raster plot of the same unit recorded during 265 randomized right turns. Bottom panel: Trial-averaged spike rate of a single unit.

C) Top panel: Right (red) and left (blue) wall positions during the OL_L turn experiment. Middle panel: spiking raster plot of a unit (animal 489, unit 489095, RS, layer 5A) recorded during 266 randomized left turns. Bottom panel: Trial-averaged spike rate of a single unit.

D) Top panel: Right (red) and left (blue) wall positions during the OL_R turn experiment. Middle panel: spiking raster plot of the same unit recorded during 265 randomized right turns. Bottom panel: Trial-averaged spike rate of a single unit.

E) Top panel: Right (red) and left (blue) wall positions during the OL_L turn experiment. Middle panel: spiking raster plot of a unit (animal 489, unit 489101, RS, layer 5B) recorded during 266 randomized left turns. Bottom panel: Trial-averaged spike rate of a single unit.

F) Top panel: Right (red) and left (blue) wall positions during the OL_R turn experiment. Middle panel: spiking raster plot of the same unit recorded during 265 randomized right turns. Bottom panel: Trial-averaged spike rate of a single unit.

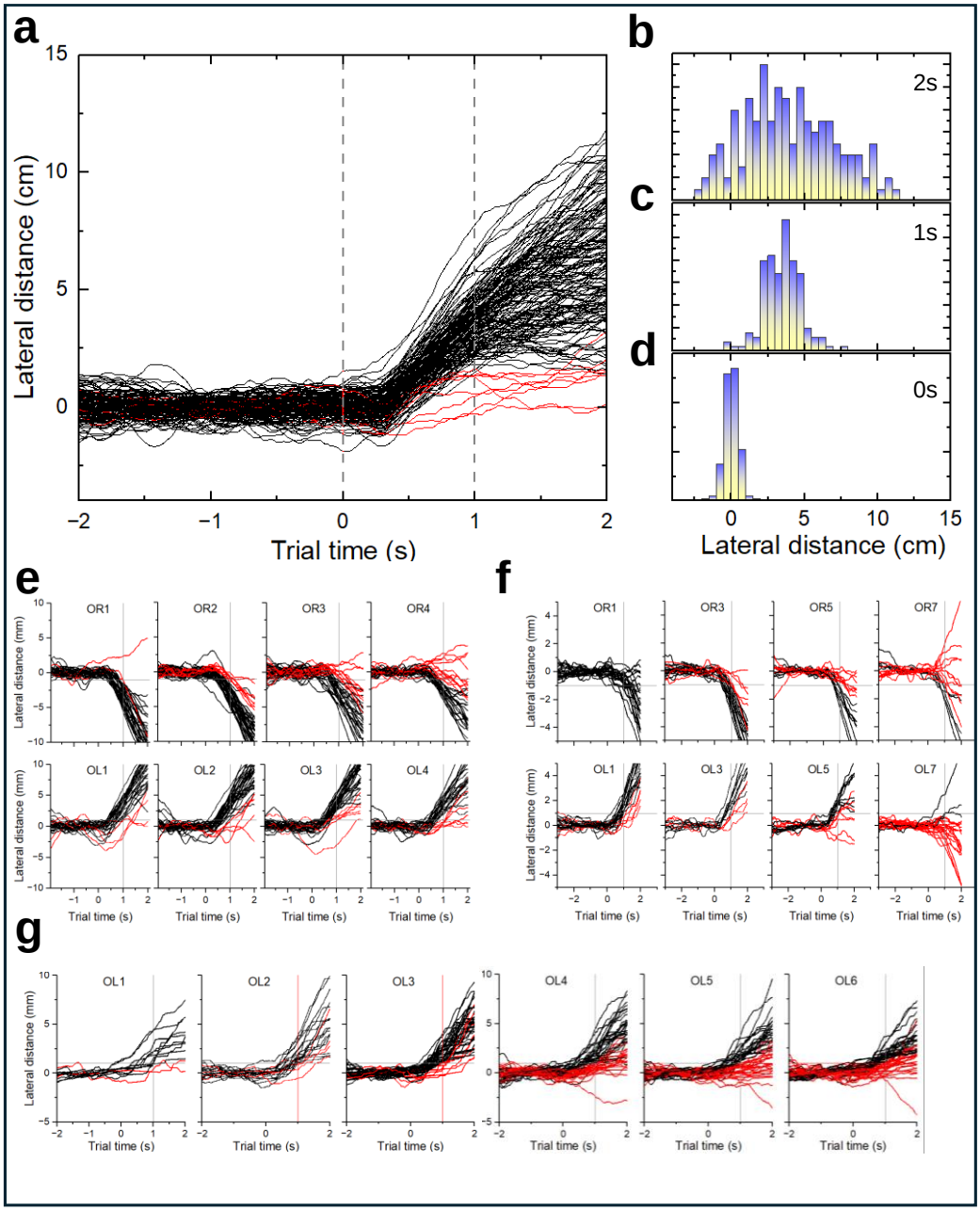

Figure 6. Examples of psychometric performance of different animals.

A) Trajectories during 520 trials with OL_L left turns (animal 489). Red curves correspond to trials assigned to decision errors.

B, C, D) Histograms of lateral distance distributions at t=0s (bottom), t=1s (middle), and t=2s (top). While at the beginning of a turn the lateral distribution is narrow, they broaden indicating gradual accumulation of navigation uncertainties.

E) Top: Trajectories during OL_R right turns (animal 474) for different distances of the wall to the snout. Red curves correspond to trials assigned to decision errors. The closer the wall is approaching the snout the less errors the animal is making. **Bottom**: Same as on top, but for OL_L left turns. Results are summarized in psychometric curves in Fig.3C, D.

F) Same as in E) for animal 499. Note very large percentage of errors at the distance of 7mm that correspond to whisker barely touching the wall during foveal whisking.

G) Same for animal 475 for OL_L left turns

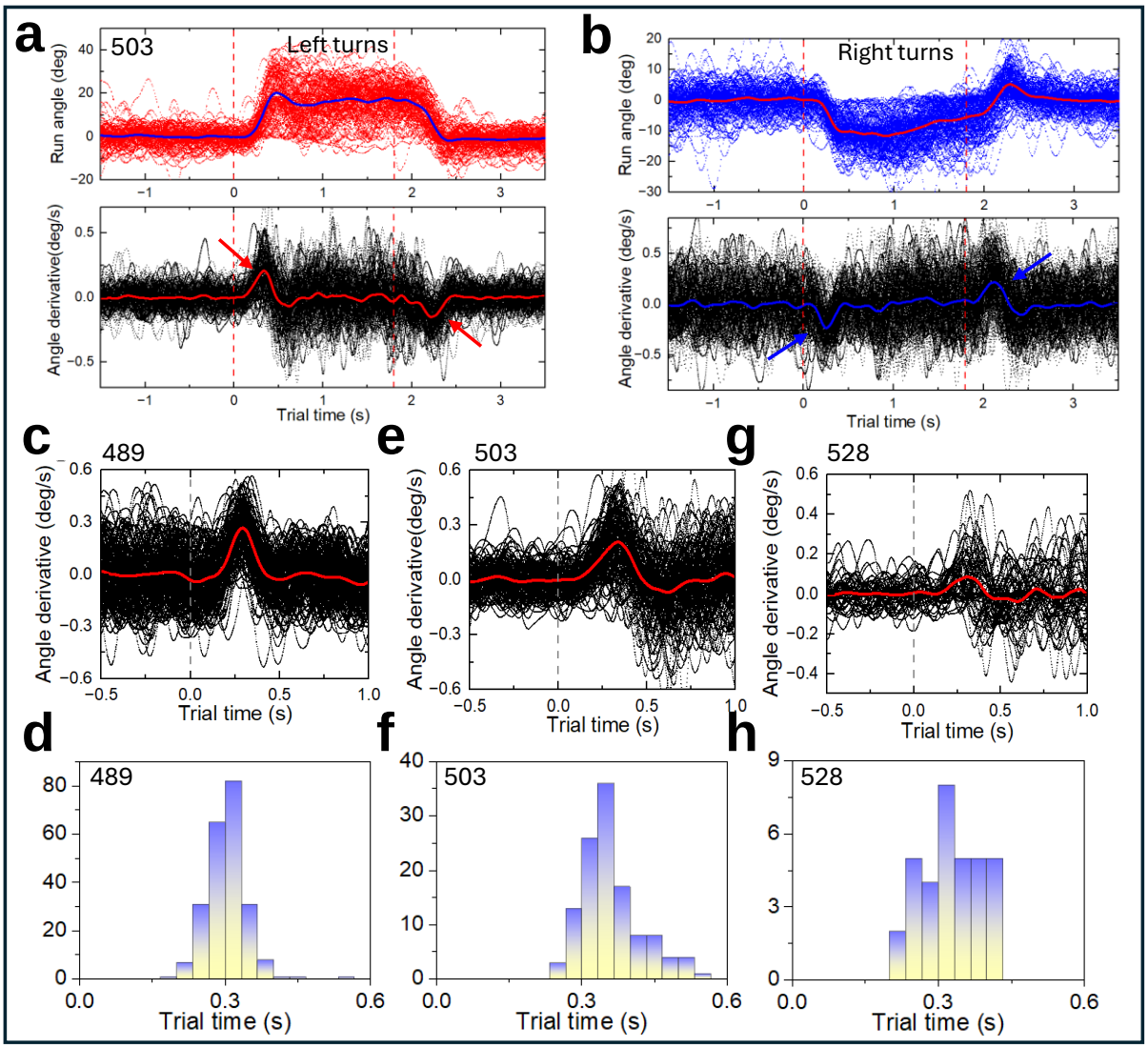

Figure 7. Procedure for extraction of reaction times.

A) Top: Run angle (animal 503) during a 305 OL_L left turn trials corresponding to data in **Fig.2A**. Blue curve is ensemble average. **Bottom**: Angle derivative for data in Top. Red curve is ensemble average. Red arrows show characteristic push by RH leg (**Fig.2G**) at the turn start and LH leg at the turn end. Vertical red dashed lines correspond to the start (t=0s) and the end (t=1.8s) of the turn.

B) Same as A) but for 304 OL_R right turns randomized with left turns in A). Blue arrows show characteristic push by LH leg (**Fig.2G**) at the turn start and RH leg at the turn end. Vertical red dashed lines correspond to the start (t=0s) and the end (t=1.8s) of the turn.

C) Run angle (animal 489) during 520 trials at the start of the left turn corresponding to data in **ED Fig.6A**.

D) Histogram of the maximum angle derivative (reaction time) for data in C).

E) Run angle (animal 503) during 305 trials at the start of the left turn corresponding to data in D).

F) Histogram of the maximum angle derivative (reaction time) for data in E).

G) Run angle (animal 528) during 95 trials at the start of the left turn.

H) Histogram of the maximum angle derivative (reaction time) for data in G).

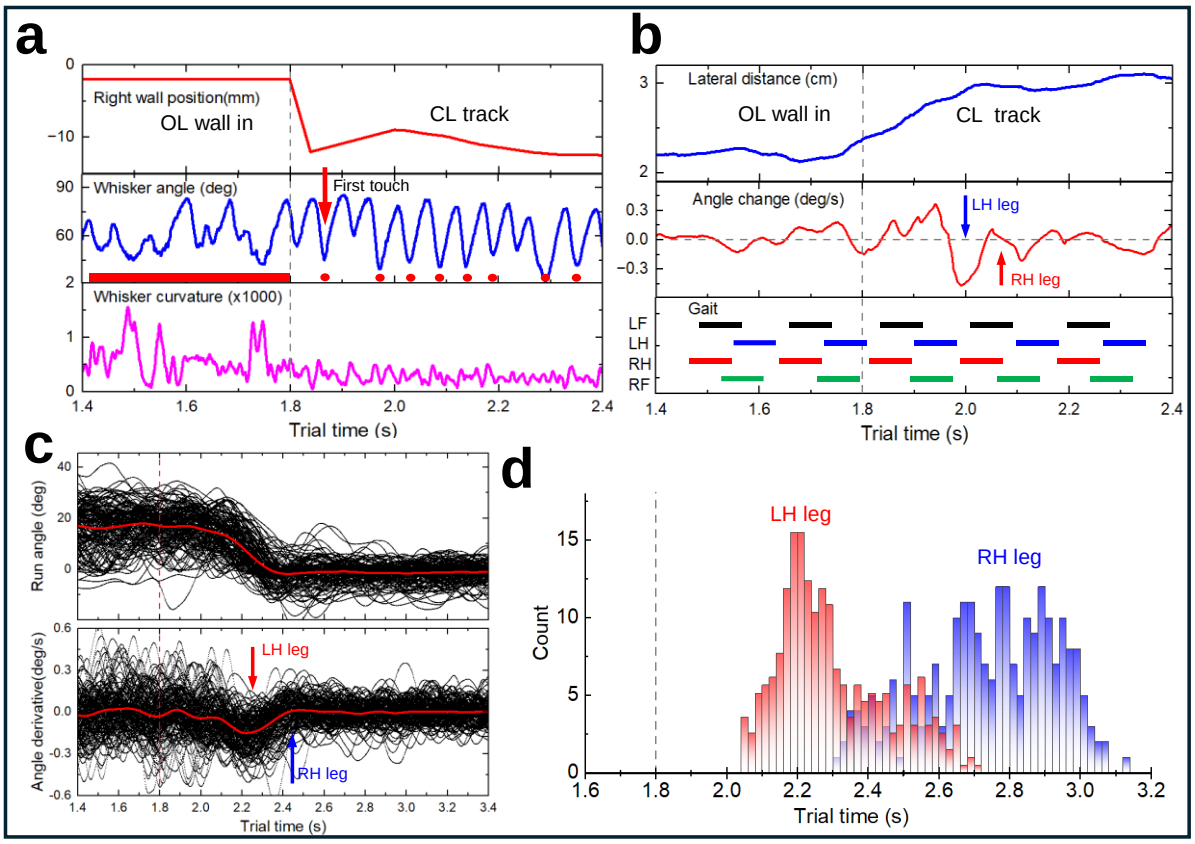

Figure 8. End of the left turn.

A) Top panel: Position of the right wall at the end of the OL_L left turn (animal 589). **Middle panel**: extracted whisker angle. Red dots identify moments of whisker touching the wall with the first touch to retracting wall marked by arrow. **Bottom panel**: Same for extracted whisker curvature. Vertical dotted line corresponds to the start of the wall movement

B) Top panel: Lateral distance during the left turn trial (animal 589). **Middle panel**: Angle change curve with a stereotypic sequence of LH leg and RH leg pushes. **Bottom panel**: tracked gait with left and right hind and fore legs following mixed walking - trotting pattern.

C) Top panel: Run angle (animal 489) during 520 trials at the end of the left turn. Red curve is ensemble average. **Bottom panel**: Angle derivative for data in Top. Red curve is ensemble average. Stereotypic sequential pushes by LH leg (red arrow) and RH leg (blue arrow). Vertical dashed line corresponds to the end (t=1.8s) of the turn.

D) Histogram of the maximum angle derivative (reaction time) for data in C).

The decision at the end of the turn is executed not by a single leg push but rather is distributed among several consecutive strides that makes RT analysis complicated. At this extended time, it is also guided by both contra- and ipsi-lateral whiskers as observed with videography and is evident from the appearance of a sharp peak at 2.1s in the ipsi-lateral right turns (**Fig.2D**).

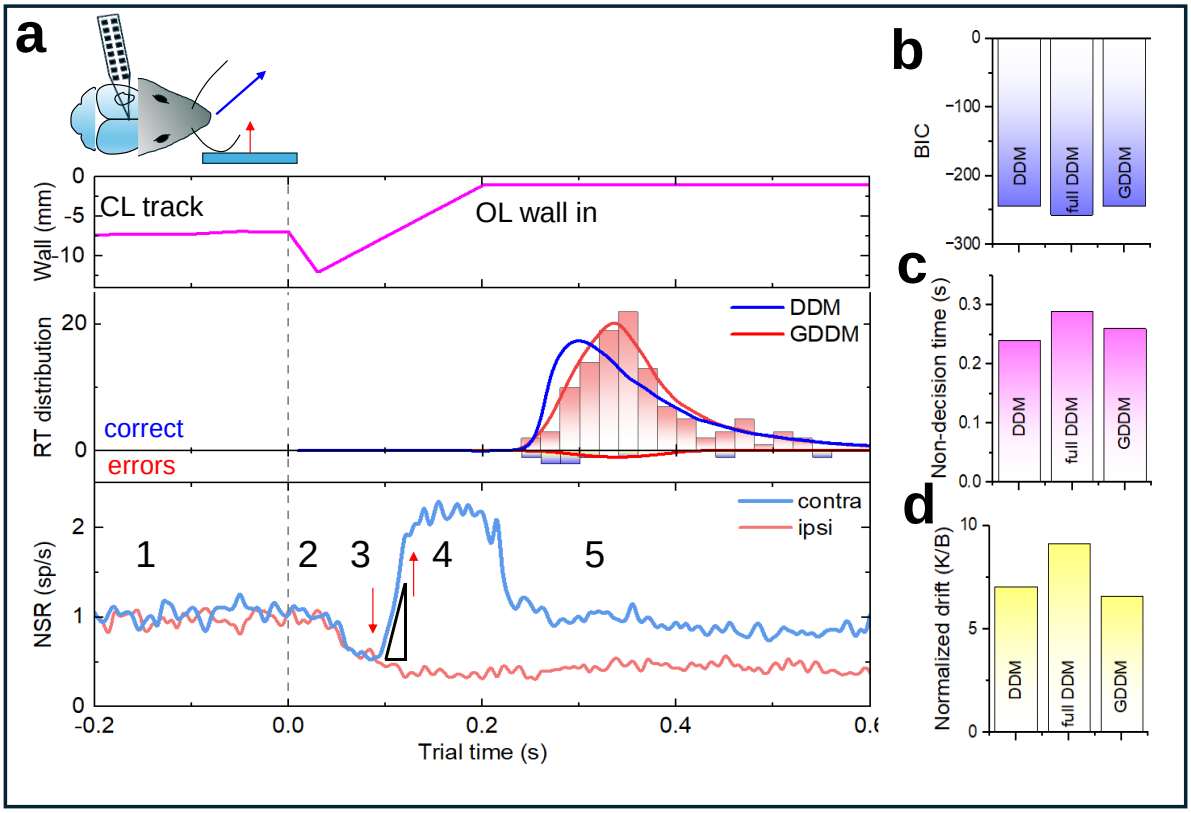

Figure 9. Ramping neural activity reflects temporal accumulation of sensory evidence.
A) Top panel: Position of the right wall during OL_L left turn trials (animal 503). **Middle**: RT distribution fitted by DDM (blue) and Generalized DDM (GDDM, red) models. **Bottom**: Normalized spike rate for contralateral (contra, blue) left and ipsilateral (ipsi, red) right turn trials. Up and down arrows denote times for the beginning and the end of the linear ramping activity. Black triangle shows linear fitting of the ramping slope.
B) Bayesian information criterion (BIC) for three fitted models – DDM, full DDM and GDDM.
C) Non-decision time derived from DDM, full DDM, and GDDM fits to the RT.
D) Drift normalized on bound derived from DDM, full DDM, and GDDM fits to the RT.

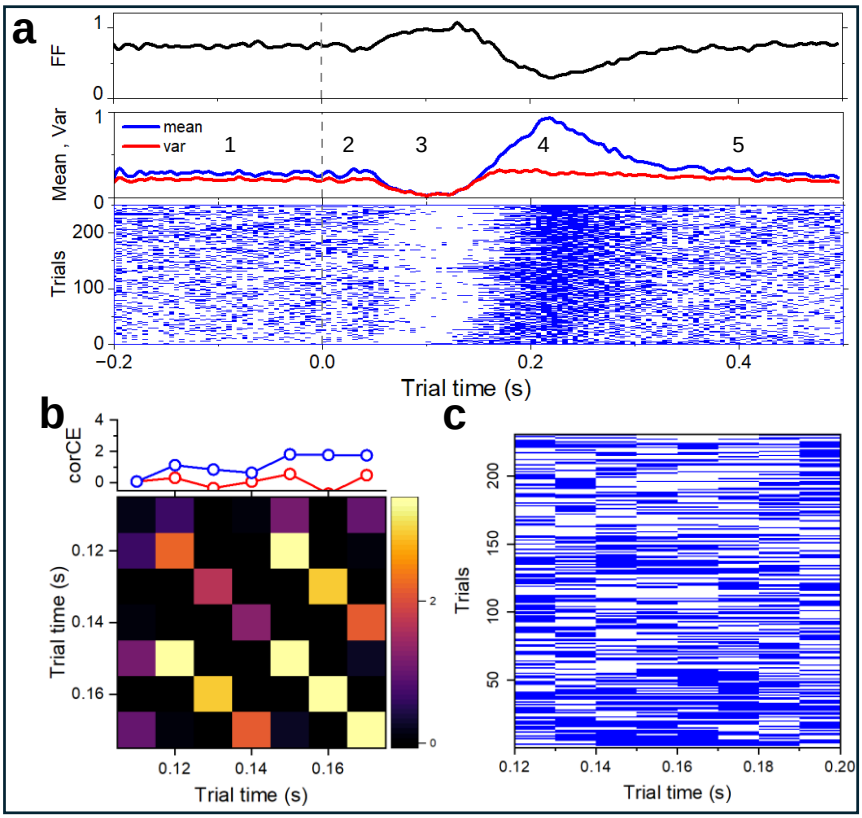

Figure 10. Noise characteristics.

A) Top panel: Fano factor for a single unit (489101, RS, layer 5A, animal 489) recorded during OL_L left turns. Middle panel: Mean (blue) and variance (red) for a single unit (489101, RS, layer 5A, animal 489). Bottom panel: Raster plot for a single unit (489101, RS, layer 5A, animal 489).

B) Covariance matrix CorCE calculated on residuals as in Fig.3J but with bins randomly shaffled. Top: corCE values along the matrix diagonal (red) and along the top row (blue).

C) Streak matrix for data in **Fig.3K**.

SUPPLEMENTARY INFORMATION

Table 1. List of mice used for behavioral and electrophysiology experiments

Animal ID	Genotype	Sex	Age	Session date	Exp type	Units	Barrel	MEA	Trials	Run %	Mean speed	Main figures	ED figures
453	Scnn1A x Ai32	F	93	9/15/2021	ephys	56	D1	CN64	2563	58.6	20.6		2
454	Scnn1A x Ai32	F	87	9/27/2021	ephys	40	D2	CN64	2581	45.4	18.4		2
456	Scnn1A x Ai32	M	94	10/1/2021	ephys	39	D2	CN64	2262	26.3	15.7		2
474	Scnn1a	M	75	5/18/2022	behavior				131	93.5	21.8	2CD	6E
475	Scnn1a	M	80	5/14/2022	behavior				55	92.5	25.4	2CD	6G
480	Scnn1A x Ai32	M	90	6/17/2022	ephys	42	C2	CN64	758	50.6	19.5	2IK, 4CE	2, 4E
482	Scnn1A x Ai32	M	96	6/24/2022	ephys	38	B2	CN64	1518	92.4	24.2	4DE	2, 4D
488	Scnn1A x Ai32	M	70	7/9/2022	ephys	29	C1	CN65	939	43.9	18.5		2
489	Scnn1A x Ai32	F	68	7/8/2022	ephys	65	C2	CN64	1000	92.6	22.2	1F-M, 3, 4BCE	2, 3, 5, 6ABCD, 7CD, 8CD, 10
499	Scnn1A x Ai32	M	72	8/22/2022	behavior				1123	95.4	19.9	2CD	6F
503	Scnn1A x Ai32	F	89	9/2/2022	ephys	48	C2	CN64	1027	52.8	16.1	1E, 2AB, 4CE	1ABC, 2, 4A, 7ABEF, 9
516	Scnn1A x Ai32	M	65	10/25/2022	ephys	33	C2		1071	72.3	17.5		2
517	Scnn1A x Ai32	F	69	10/27/2022	ephys	42	C3	CN64	1287	73.9	23.2	4DE	2, 4F
518	Scnn1A x Ai32	F	90	11/18/2022	behavior				1291	93.9	22.2	2CD	
528	Scnn1A x Ai32	M	112	2/1/2023	ephys	89	C2	NP1.0	525	96.2	21.3	4CE	2, 4B, 7GH
530	Scnn1A x Ai32	M	105	20/9/2023	ephys	113	C1	NP1.0	1654	93.4	24.2	4DE	2, 4C
573	Scnn1a	M	78	5/17/2024	behavior				401	68.6	16.4	2EFI	
579	Scnn1A x Ai32	F	81	7/3/2024	ephys	34	C2	NP1.0	55	51.3	15.5	2J	2
589	Scnn1A x Ai32	F	90	11/7/2024	behavior				50	87.2	17.2	2GH	8AB
					Total:	668							

* Number of single units sorted and passed through acceptance criteria.
* Number of trials: Total number of trials including CL straight, randomzied left and right turns.
* Animal age is in postnatal days P
* Mean speed for all trials in cm/s when mouse is running (>10cm/s)
* Run % corresponds to percentage of trials during the main session with mean speed above 10cm/s
* NP1.0 stands for Neropixels 1.0 probes, CN64 stands for Cambrdige Neurotech 64 channels probes.

Table 2. Parameters of models best fitted to RT data Fig.3B (animal 489)

Parameter	DDM	full DDM	GDDM
Animal	489	489	489
drift	2.91	2.81	9.56
noise	0.25	0.1	1.29
B	0.59	0.54	0.86
x0		0.01	0.01
xo width		0.04	0.01
ndt	0.11	0.12	0.14
ndt width		0.05	0.07
leak			170.68
tau			6.07
drift/B	4.93	5.20	11.12
BIC	-664	-666	-705

Table 3. Parameters of models best fitted to RT data ED Fig.9 (animal 503)

Parameter	DDM	full DDM	GDDM
Animal	503	503	503
drift	2.54	1.46	2.77
noise	0.75	0.48	0.87
B	0.36	0.16	0.42
x0	0.01	0.04	0.03
xo width		0.01	0.04
ndt	0.24	0.29	0.26
ndt width		0.09	0.26
leak			1.15
tau			2.31
drift/B	7.06	9.13	6.61
BIC	-244	-257	-244

Video 1

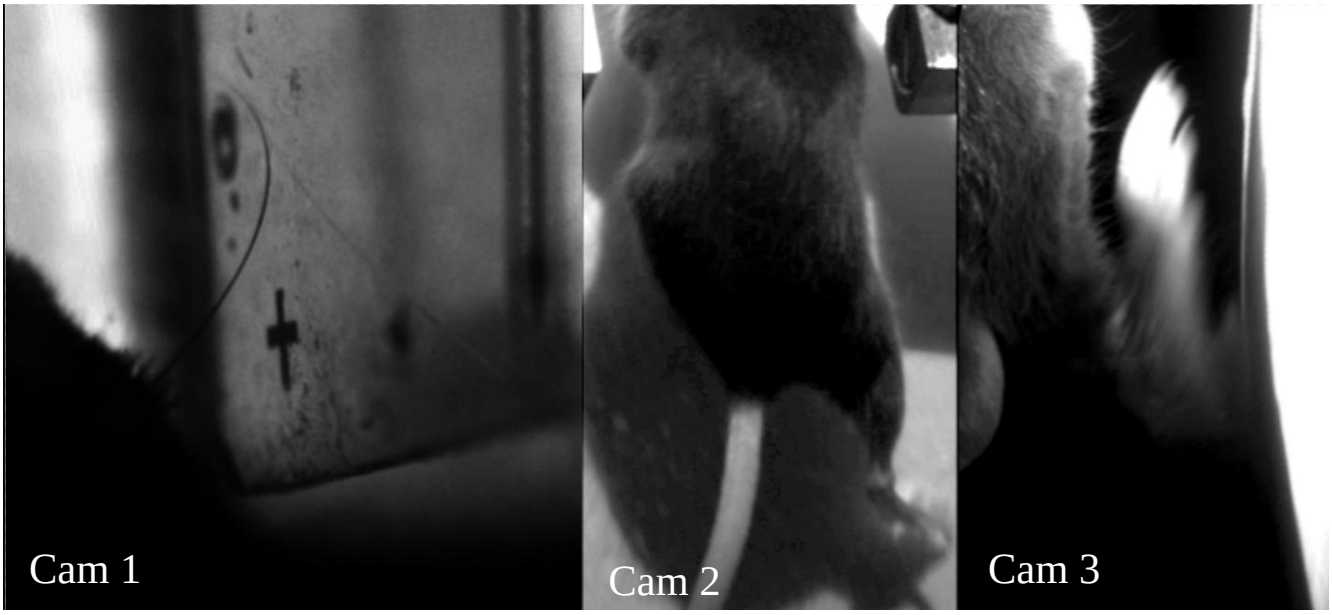

Video 1. The video combined with 3 cameras showing synchronized video streams from whisker recording (cam 1) together with recordings of hind (cam 2) and fore (cam 3) legs during whisker-guided navigation.